RESEARCH ARTICLE

Hovering flight in hummingbird hawkmoths: kinematics, wake dynamics and aerodynamic power

Kajsa Warfvinge, L. Christoffer Johansson and Anders Hedenström*

ABSTRACT

Hovering insects are divided into two categories: 'normal' hoverers that move the wing symmetrically in a horizontal stroke plane, and those with an inclined stroke plane. Normal hoverers have been suggested to support their weight during both downstroke and upstroke, shedding vortex rings each half-stroke. Insects with an inclined stroke plane should, according to theory, produce flight forces only during downstroke, and only generate one set of vortices. The type of hovering is thus linked to the power required to hover. Previous efforts to characterize the wake of hovering insects have used low-resolution experimental techniques or simulated the flow using computational fluid dynamics, and so it remains to be determined whether insect wakes can be represented by any of the suggested models. Here, we used tomographic particle image velocimetry, with a horizontal measurement volume placed below the animals, to show that the wake shed by hovering hawkmoths is best described as a series of bilateral, stacked vortex 'rings'. While the upstroke is aerodynamically active, despite an inclined stroke plane, it produces weaker vortices than the downstroke. In addition, compared with the near wake, the far wake lacks structure and is less concentrated. Both near and far wakes are clearly affected by vortex interactions, suggesting caution is required when interpreting wake topologies. We also estimated induced power (P_{ind}) from downwash velocities in the wake. Standard models predicted a P_{ind} more than double that from our wake measurements. Our results thus question some model assumptions and we propose a reevaluation of the model parameters.

KEY WORDS: *Macroglossum*, Aerodynamics, Flight model, Hovering, Particle image velocimetry, Vortex wake

INTRODUCTION

Hovering is a flight mode utilized by all major extant flying taxa, and most commonly found in nectar-feeding species. Among birds, only hummingbirds are able to hover sustainably, while several species of bats, mainly the nectar-feeding and gleaning species, are able to do so. In insects, however, hovering is a ubiquitously used flight mode. Based on airplane theory, it has been suggested by Pennycuick (1968), for example, that the relationship between power required to fly and flight speed follows a U-shaped function, so that very slow (e.g. hovering) and very fast flight require more power than flight at intermediate speeds. Empirical data have supported this relationship for vertebrates (see e.g. Engel et al., 2010). However, it has historically been surmised that insects – operating in a different flow regime from birds and bats – are exempt from the problem of costly hovering, and several empirical studies have suggested that hovering requires a similar amount of power as forward flight (e.g. see Ellington et al., 1990 on bumblebee flight). Yet, studies using quantitative flow measurements to determine the cost of hovering in insects are lacking.

The reason for a costly flight in hovering can be found in how aerodynamic forces are generated in animals. If hovering, there is no oncoming air to assist the wing to generate lift, and with a completely symmetrical wingbeat, where stroke reversal is not accompanied by any change in the wing's attitude, the upstroke would produce the undesirable effect of equal but opposite forces to that of the downstroke, thus grounding the animal. To solve this problem, two general approaches – constrained by morphology and angular mobility of the joints associated with the wing – can be used. The first is to make the upstroke aerodynamically inactive. Birds, except hummingbirds, accomplish this by folding the wing to reduce the wing area and by aligning the wing to the air moving across the wing – so-called feathering – to minimize drag and lift (e.g. Muijres et al., 2012a,b; Norberg, U. M., 1975). Alternatively, the upstroke can be made useful by, for example, rotating and/or twisting the wing to change the angle to the oncoming air, allowing the wing to generate lift to support the weight. This is the strategy employed by hummingbirds, who do not to any considerable extent retract their wings (Warrick et al., 2005), and to some extent by bats that flip their wings upside-down, but perform some wing retraction (Håkansson et al., 2015). Among insects, which lack the ability to fold their wings, the choice of strategy has been suggested to be related to the angle of the wing's stroke plane (Ellington, 1984b). Species employing 'normal hovering' move their wings in a horizontal plane, where the wing tip typically follows a horizontal figure-eight pattern when viewed from the side, and the wing is rotated at the base to adjust the angle relative to the air. This has been suggested to result in equally high lift production during both half-strokes, with a thrust of equal magnitude, but opposite sign, during downstroke and upstroke (Weis-Fogh, 1973). With an inclined stroke plane angle in insects (e.g. dragonflies; Norberg, R. Å., 1975), they should instead produce lift mostly during downstroke and rotate the wing to feather the upstroke.

Evidence of how alternative wing movements (and morphology) affect the air flow can be found by studying the vortex wake behind (or, in the case of hovering, below) the flying animal; in recent times often by using particle image velocimetry (PIV) (e.g. see Henningsson et al., 2015; Håkansson et al., 2015; Johansson et al., 2016; Warfvinge et al., 2017; and for a review, see Bomphrey, 2012). Simplistically, the wake generated by a hovering animal could be described as a number of vortex rings travelling downwards by their own induced velocity

Department of Biology, Ecology Building, Lund University, SE-223 62 Lund, Sweden.

*Author for correspondence (anders.hedenstrom@biol.lu.se)

K.W., 0000-0003-1038-8953; L.C.J., 0000-0002-1851-3635; A.H., 0000-0002-1757-0945

List of symbols

|	
A	wake area
A_0	disk area
$\hat{c}$, $c(r)$	local wing chord
E	kinetic energy
e_{span}	span efficiency
f	wing beat frequency
F_T	thrust
f_v	frequency of wake shedding
$\boldsymbol{g}$	acceleration due to gravity
J	advance ratio
k, k_{span}	induced drag factor
L	lift
m	mass
$\dot{m}$	mass flow rate
p	momentum
P	power
p_d	disk loading
P_{ind}	induced power
$P_{ind,ideal}$	ideal induced power of actuator disk
R	wing length
R_2	second moment of area
S	wing area
T	wingbeat period
w	wake velocity (final)
w_0	induced velocity
β	body angle
γ	elevation angle
θ	stroke plane angle
ρ	air density
σ	spatial correction factor
τ	temporal correction factor
φ	positional angle of wing in the stroke plane
ϕ	wing stroke amplitude
ω_z	vorticity about the z-axis
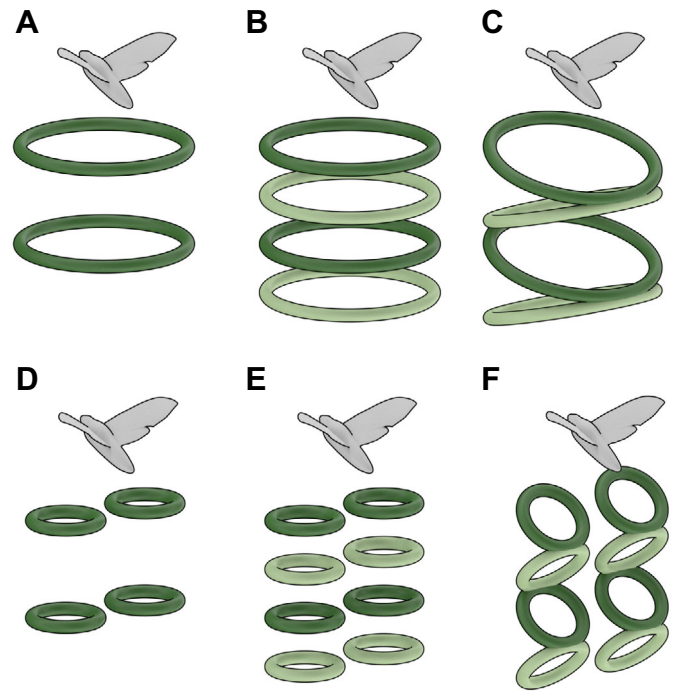
Fig. 1. Cartoon representation of five different wake topologies. Dark green vortex rings are created as a result of the downstroke, and light green rings during upstroke. In A–C, the body and both wings actuate in such a way that one vortex ring is generated from the whole configuration. In D–F, each wing produced its own vortex ring. E and F are identical except for the fact that the rings produced during downstroke and upstroke are coupled and tilted in F, representing thrust production during the downstroke and negative thrust during the upstroke.

(see Fig. 1 for a cartoon representation of alternative wake models). A flier with an active upstroke should produce a ring during each half-stroke (Fig. 1B,C), while one with an inactive upstroke only produces one ring per wingbeat – during the downstroke (Fig. 1A). In hovering flight, the flow over the body is very low (if not zero), and so it is likely that the body is aerodynamically inactive (Pournazeri et al., 2013). Then, vorticity is released from the base of the wing, which leads to a formation of one vortex ring per wing (bilateral rings, Fig. 1D–F), instead of one large ring being released from the full wingspan. While work on bats has shown that the wakes of hovering animals can be much more complex than these simple models (Håkansson et al., 2015), it can still be useful to attempt to categorize wakes in this way for a convenient comparison among taxa (see Fig. 1) and for simplified modelling of flight costs. Among vertebrates, non-trochilid birds, having an asymmetric wingbeat, have been proposed to produce one vortex ring per wingbeat (e.g. pied flycatcher *Ficedula hypoleuca* studied in slow flight; Muijres et al., 2012a). Hummingbirds, in contrast, release rings during both downstroke and upstroke, where the upstroke is responsible for ~25–35% of the lift (Altshuler et al., 2009; Ingersoll and Lentink, 2018; Warrick et al., 2005; Wolf et al., 2013). A nectar-feeding bat has also been shown to produce bilateral rings each half-stroke, demonstrating an active upstroke, although with weaker vortices being shed during upstrokes (Håkansson et al., 2015).

Early studies using low-resolution techniques such as smoke and dust flow visualization disagreed on whether insects in general should produce vortex rings during downstroke only (Grodnitsky and Morozov, 1993) or during both half-strokes (Brodsky, 1994). However, with time-resolved PIV, this open question can now be

addressed. In the present study, we focused specifically on the hovering of hawkmoths, a family often used in insect flight studies. Several attempts have previously been made to characterize the wake topology of these insects. In an experiment using a mechanical flapper based on the morphology and downstroke kinematics of a hovering *Manduca sexta*, van den Berg and Ellington (1997) used smoke visualizations to show separate vortex rings being shed from each wing, moving away from each other in the near wake. The authors suggested that the two rings could, further down in the wake, merge into one structure if the root vortices cancel (although they found this unlikely). Similarly, in computational fluid dynamics (CFD) simulations of a hovering hawkmoth, Aono et al. (2009) implied a wake topology of bilateral, separated vortex rings. However, in this case, the wake originated as one full-span ring that subsequently broke up into two. The topology as well as the magnitude of the induced velocities were similar during both half-strokes, indicating a relatively symmetric wingbeat. Whether or not the bilateral vortex rings should move apart or merge into one, larger ring was suggested by Liu and Aono (2009) to be related to the size of the animal. In their CFD study of four types of insect (thrips, fruit fly, honeybee and hawkmoth), Liu and Aono (2009) demonstrated that smaller species produced rings moving away from each other, while in a large hawkmoth the two rings produced by each wing merged to form a wake structure more similar to a one-ring model. Knowing the structure of the wake is not only esoteric knowledge because mathematical models of aerodynamic power often assume a specific wake topology, and knowing the approximate structure of the wake helps inform the decision on whether any of the proposed models could be applicable.

Although insect hovering has been simulated using CFD (e.g. Aono et al., 2009; Cheng and Sun, 2016; Liu and Aono, 2009) and studied using mechanical flappers (e.g. van den Berg and Ellington, 1997; Fry et al., 2005; Cheng et al., 2014), to the best of our knowledge, there has yet to be conducted a quantitative PIV study showing the wake of a live, non-tethered, hovering insect. However, in a recent PIV study of *M. sexta*, the hawkmoths flew as slowly as 1 m s^{-1} (advance ratio J=0.27), and at this speed displayed no signs of an active upstroke, as only vorticity released during the downstroke was visible in the wake visualizations (Warfvinge et al., 2017). Root vortices were found but did not connect to the tip vortices to form clear rings. Contrary to this, schlieren photographs of the wake of near-hovering *M. sexta* have suggested that the moths in fact produce connected vortex rings during both half-strokes, one from each wing (Liu et al., 2018). Despite long being categorized as a 'normal hoverer' (Weis-Fogh, 1973), *M. sexta* has a stroke plane angle of approximately 35 deg at 1 m s^{-1}, which makes inactive upstroke hovering a plausible model according to Ellington (1984b).

Knowing the cost of flight has implications for our understanding of ecological phenomena as well as morphological adaptations to flight. Several models of animal flight power have been developed, most incorporating the idea of the actuator disk (helicopter model), which is an infinitesimally thin disk through which air is accelerated to produce lift. The disk is an ideal structure, producing lift in the most efficient way possible, but flying animals are obviously subject to inefficiencies of several kinds. Models have countered this problem in different ways. Pennycuick (1968; vertebrates) and Willmott and Ellington (1997; insects) used a general correction factor (k) to account for all inefficiencies generated by the animal, and this coefficient has to be experimentally determined for the model to be useful. These models have been used to predict power in forward flight as well as hovering. As noted above, hovering is special because all aerodynamic force and power comes from the flapping motion of the wings. An alternative approach to model power, developed by Ellington (1984a,b,c) specifically for insect hovering, is to more realistically model the structure of the vortex wake using kinematic parameters, and from this derive the required power. These models are thus dependent on a number of assumptions that need to be evaluated.

Here, we studied the hovering of a relatively small hawkmoth: *Macroglossum stellatarum* (Linnaeus 1758). Being closely related to *M. sexta*, we expected its vortex wake to show the signs of a more asymmetric hovering. Considering its smaller size, we found it likely that should the moths produce bilateral rings, these would not merge to form a larger ring. In addition to determining whether its vortex wake can be categorized as one of the aforementioned models (Fig. 1), we sampled the wake at two different distances from the animal, in an attempt to characterize the wake evolution. Because the aerodynamic performance of the animal at hovering flight is entirely dependent on the movement pattern of the wings, we expected performance and wake structures to be linked to kinematics. We therefore tracked wing and body movements to investigate potential effects of kinematics on wake topology. In addition, we used the kinematics and PIV data to evaluate Ellington's (1984a,b,c) vortex model's ability to estimate the power required for insect hovering.

MATERIALS AND METHODS
Using tomographic particle image velocimetry (tomo-PIV), we recorded air flow generated by five specimens of the day-active hummingbird hawkmoth during hovering. The resulting vector fields were used for both flow visualizations and to estimate

aerodynamic power – the latter results were used to evaluate Ellington's (1984a,b,c) model. Simultaneously with the PIV measurements, kinematics measurements were recorded with a stereo camera setup. These measurements were used as input into aerodynamic power models, as well as to investigate the potential link between kinematics and vortex wake topology.

Study species and experimental regime
Five hawkmoths, acquired as pupae and hatched in the laboratory, were trained to feed from an artificial blue flower. As the day-active species stays inactive in dark conditions, the wing wear could be reduced by keeping the moths in small paper boxes overnight. Each moth was, in turn, released into the Lund University animal flight wind tunnel (Pennycuick et al., 1997) at a wind speed of 0.1–0.3 m s^{-1}. This speed allowed for the smoke fluid used as tracer particles for PIV measurements to mix with the air, while at the same time being low enough that the moths were considered to be hovering by Ellington's (1984a) definition (advance ratio $J{\approx}0.048$, $J_{hover}{<}0.1$).

When a moth was hovering stably in front of the feeder, a recording was triggered, lasting approximately 3 s. The moths rarely reacted noticeably to the laser light, but when a reaction was visible in the data, this section of the recording was discarded. Thirty flight sequences were recorded, but in both the kinematics and PIV datasets, four (different) sequences were discarded owing to suboptimal placement of the moth or the wake, respectively. In total, 2975 stable wingbeats were recorded with PIV. Of these sequences, 20 were recorded with the moth approximately 40 mm (~5 chord lengths) above the laser sheet, while in the remaining six sequences (using two different individuals) the sheet was instead positioned 140 mm (~18 chord lengths) below the animal. This allowed us to study the evolution of the vortex wake when it travels downwards after being shed from the wings and body, and whether power measurements are affected by the distance from the animal and measurement plane. All averages and standard deviations are calculated with data from the default feeder placement (40 mm below the animal), if not otherwise explicitly stated. Body weight and morphological characteristics of the moths used in the study are shown in Table S1.

Experimental setup and PIV
Kinematics were recorded with two high-speed cameras (HighSpeedStar 3, 1024×1024 pixels, 1000 Hz) (see Fig. S1). For a time-resolved 3D-characterization of the wake, a tomo-PIV system from LaVision GmbH, recorded air flow at 640 Hz. The system consisted of a 527 nm Nd-YLF double-cavity laser (Litron Lasers Ltd, model LDY304PIV) and four high-speed cameras (Imager Pro HS 4, 2016×2016 pixels), and was seeded with a mist of Di-Ethyl-Hexyl-Sebacat smoke fluid. Because the wake of a hovering animal travels downwards, the laser sheet was aligned horizontally, and the cameras were placed below the tunnel aiming up at the sheet (Fig. S1).

A right-handed coordinate system was defined, where x and y are parallel and perpendicular to the free-stream, respectively, and z is parallel to gravity.

PIV analysis was performed using DaVis 8.3 (LaVision GmbH) with the following settings: image preprocessing (subtract sliding minimum, normalize with local average, Gaussian smoothing, sharpening, multiply each pixel with factor 10), volume reconstruction (fast MART), and volume correlation (direct correlation, decreasing correlation window sizes from 96 to 32 pixels with 50% overlap, multi-pass post-processing with universal outlier detection and smoothing 3×3×3 pixels). Postprocessing (remove vectors with correlation coefficient <0.3, universal outlier detection,

smoothing 3×3×3 pixels) was applied to the resulting vector fields. This resulted in 128×129×3 vectors with a 1.3 mm vector spacing, from where only the centre plane in z was used. Subsequent analysis was done with custom MATLAB (R2017a, MathWorks) and R (3.4.4, https://www.r-project.org/) scripts.

Visualizations of the flow were created by stacking the centre plane of each vector field to form a quasi-3D volume. The distance between the planes was calculated from the average induced velocity in each sequence. For each of the constructed volumes, we calculated the Q-value, which is a component of the flow used for identifying vortex structures (where $Q>0$; Kolář, 2007). Computing Q in this way created clearer visualizations than when it was calculated directly from each tomo volume. This is possibly due to difficulties determining the velocity gradients in flow direction when only using three planes with overlap. However, thin-volume tomo-PIV has been shown to reduce systematic errors in the out-of-plane velocities when compared with stereo-PIV (Scarano, 2013), which is why a tomographic analysis was used on the very thin volumes.

Kinematics

Two kinematics cameras were calibrated using MATLAB's computer vision system toolbox and an asymmetric checkerboard pattern (average calibration error: 0.7 pixels). For each of the 26 recorded flight sequences that had the moth fully in view, 100 frames were manually digitized with four points in each frame and camera view (wing tip, wing base, the most anterior and posterior points of the body). These were triangulated to 3D coordinates in the wind tunnel coordinate system. The start and stop positions of a wingbeat were automatically detected by tracking the x and z positions of the wing tip and finding peaks in the cyclic signals using the R (3.4.4, https://www.r-project.org/) function findpeaks (minimum peak distance=10 frames). Here, z_{min} represented the start of downstroke, while x_{max} was used to detect the start of upstroke (Fig. S2A). A variable (τ) representing the normalized time during a wingbeat was then defined.

Owing to the very low airspeed of the wind tunnel, the moths did not always line up their body with the oncoming airflow. Therefore, we rotated the coordinate system so that the horizontal component of the head-to-tail vector was parallel to the x direction.

Kinematic parameters were then calculated from the point data, some of them only for later use in Ellington's (1984b) model. Stroke plane angle (θ) and body angle (β) were both defined with respect to the horizontal (Fig. 2). Stroke angle (φ) was defined as the instantaneous angle between the wing base-to-wing tip vector and a vector perpendicular to the body axis, in the stroke plane (see

Fig. 2). Then, stroke amplitude (Φ) could simply be calculated as $\varphi_{max}-\varphi_{min}$, and angular velocity ($d\varphi/dt$) by differentiating φ with respect to time. Elevation angle (γ) was calculated as the angle of the wing base to tip vector to the stroke plane in a plane aligned with the vector and perpendicular to the stroke plane. One video frame per individual, where the moth had its wings fully outstretched, was used to measure wing area (S), wing length (R) and, in 100 steps along the wing, local wing chord [$c(r)$].

Modelling hovering power
The actuator disk

When studying the flight forces and power of a hovering animal, a useful approach is to turn to helicopter theory. Here, we find the actuator disk; a simplified model for calculating forces and power of rotating wings (see Gessow and Myers, 1952 for a derivation of relevant equations). The actuator disk is a theoretical circular disk of uniform pressure difference that accelerates air through its surface. Far above the disk the air is stationary, at the disk the induced velocity is w_0 and far below the disk the air has reached its final velocity of $w=2w_0$. The area (A_0) of the disk is the area swept by the rotating wings, and, owing to conservation of momentum, the area in the far wake (A) has contracted to half the size of the disk.

The lift (L) produced by the actuator disk during one time unit is the difference in momentum (Δp, defined as mass times velocity) between the still air above the disk and the far wake, calculated as:

$$L = \frac{\Delta p}{t} = \frac{mw - 0}{t} = \dot{m}w, \quad (1)$$

where $\dot{m}$ is the mass flow rate of air through an area that can be calculated at the actuator disk or the far wake as:

$$\dot{m} = \rho A_0 w_0 (\text{disk}). \quad (2)$$

$$\dot{m} = \rho A w (\text{far wake}). \quad (3)$$

Depending on choice of measurement location, lift then becomes:

$$L = \rho A_0 w_0 w = 2\rho A_0 w_0^2 (\text{disk}). \quad (4)$$

$$L = \rho A w^2 (\text{far wake}). \quad (5)$$

Similarly, we can calculate the power (P) required to produce this lift from the difference in kinetic energy (E) between the still air and the far wake:

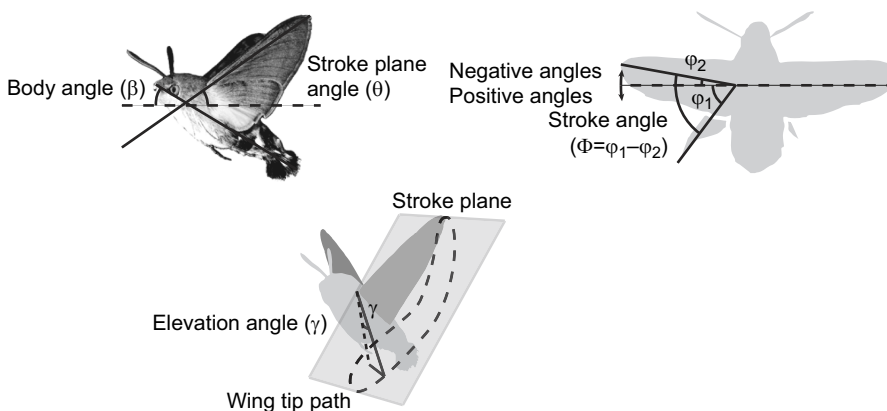$$P = \frac{\Delta E}{t} = \frac{1}{2}\dot{m}w^2. \quad (6)$$

Fig. 2. Definition of the kinematic parameters body angle (β), stroke plane angle (θ), instantaneous stroke angle (φ), stroke angle/amplitude (Φ) and elevation angle (γ).

Finally, power can be calculated from the disk or far wake as:

$$P = \frac{1}{2}\rho A_0 w_0 w^2 = 2\rho A_0 w_0^3 \text{(disk)}. \tag{7}$$

$$P = \frac{1}{2}\rho A w^3 \text{(far wake)}. \tag{8}$$

Modifications for animal flight

Pennycuick (1968) modified the actuator disk model for vertebrate flapping flight by defining the disk area as a circle with diameter of the animal's wingspan. To account for the unrealistic assumptions of a uniform downwash (downwards-directed flow), the author used a correction, the induced power factor k, somewhat arbitrarily set to 1.2. k is the ratio between the actual and ideal induced power, so that:

$$P_{\text{ind}} = k P_{\text{ind,ideal}}, \tag{9}$$

where $P_{\text{ind,ideal}}$ is the ideal power produced by a disk of uniform downwash (see Eqn 7). k is sometimes defined as the instantaneous ratio between the measured and ideal power and is then equal to the inverse of the span efficiency (e_{span}; Spedding and McArthur, 2010). For the purpose of having a consistent definition throughout this paper, we have used k as a 'catch-all' correction for all deviations from the ideal produced throughout the wingbeat, and k_{span} if only the instantaneous deviations are taken into account.

k has been experimentally estimated for multiple species (*M. stellatarum*: k_{span}=2.17, Henningsson and Bomphrey, 2013; desert locust: k_{span}=1.89, Henningsson and Bomphrey, 2012; pied flycatcher: k=1.22 and k_{span}=1.11, Muijres et al., 2012a; Pallas' long-tongued bat: k_{span}=1.23, Muijres et al., 2011; lesser long-nosed bat: k=1.69, Håkansson et al., 2015 and k_{span}=1.27, Muijres et al., 2011).

Ellington's model

In a series of papers, Ellington (1984a,b,c) used the actuator disk as a basis for a more realistic, kinematics-based model of hovering insect flight. The first modification is to the area of the disk. Instead of assuming a circular disk with the wingspan as diameter (*sensu* Pennycuick, 1968), a horizontal projection of the area swept by the wings is used:

$$A_0 = \Phi R^2 \cos\theta, \tag{10}$$

where Φ is the angle the wing sweeps, R is wing length and θ is stroke plane angle. Assuming the lift exactly balances the weight ($m\boldsymbol{g}$) of the animal, the ideal induced power becomes (Ellington, 1984b):

$$P_{\text{ind,ideal}} = \frac{(m\boldsymbol{g})^{3/2}}{\sqrt{2\rho A_0}}. \tag{11}$$

Second, a spatial correction factor σ is introduced to account for non-uniform induced velocities across the disk. This is similar to the k_{span} in Henningsson and Bomphrey (2013). The correction factor uses measurements on the normalized local chord $\hat{c}$ and wing length $\hat{R}$ as well as the normalized angular velocity $d\tilde{\varphi}/d\hat{t}$ and non-dimensional radius of the second moment of wing area $\hat{R}_2(S)$ (for details, see Ellington, 1984a,b,c):

$$\sigma = \frac{\sqrt{2}\overline{|d\tilde{\varphi}/d\hat{t}|^{5/2}} \int_0^1 \hat{c}^{3/2}\hat{R}^{5/2}d\hat{r}}{\hat{R}^{3/2}(S)\left(\overline{(d\tilde{\varphi}/d\hat{t})^2}\right)^{3/2}} - 1. \tag{12}$$

Additionally, Ellington recognized that the wake of a hovering insect is not a continuous jet but has a pulsed nature owing to the cyclic flapping motion of the wings. The model assumes that an insect with an inclined stroke plane produces one pair of vortex rings each wingbeat. A species employing normal hovering should instead produce a vortex pair on the upstroke as well as the downstroke, so that the frequency of vortex shedding is twice the wingbeat frequency (f_{v}=2f). Following Ellington (1984a), we defined the hovering flight of *M. stellatarum* as inclined stroke plane based on the measured stroke plane angle of approximately 33 deg (present study). In the ideal situation, vortex rings are produced with an infinite frequency, and the longer the spacing between the rings, the less efficient is the force production. A temporal correction factor τ is defined as:

$$\tau = 0.079\frac{2\pi p_{\text{d}}}{\rho A_0 f_{\text{v}}^2}, \tag{13}$$

where p_{d} is the disk loading (see Ellington, 1984b,c for details as well as a justification for the constant 0.079).

Finally, the spatial and temporal corrections are added, and the induced power is simply calculated as:

$$P_{\text{ind}} = P_{\text{ind,ideal}}(1 + \sigma + \tau). \tag{14}$$

Note that in these papers, Ellington (1984b,c) defines k as 1+τ, so that it only represents the temporal correction. For ease of comparison, we have chosen to see k as a correction to both temporal and spatial factors, and it is thus hereafter defined as k=(1+σ+τ).

Power measurements from the wake

From the PIV data, we obtained information about the real flow velocities in the wake as well as the cross-sectional wake area. We can therefore calculate the induced power without any assumptions about the geometry of an ideal disk by integrating the following equation (based on Eqn 8) over a wingbeat and the measured wake area:

$$P_{\text{ind}} = \frac{1}{T}\frac{\rho}{2} \int_{\text{wb}} \int_{A(t)} \int w(x,y,t)^3 dxdydt, \tag{15}$$

where t is the time during a wingbeat (wb) and T is the wingbeat period. Similarly, lift produced during one wingbeat is calculated as:

$$L = \frac{1}{T}\rho \int_{\text{wb}} \int_{A(t)} \int w(x,y,t)^2 dxdydt. \tag{16}$$

Both P_{ind} and L are first calculated for each frame, and then averaged over a wingbeat.

We can now calculate k from Eqn 9 by first determining the uniform downwash w that would result in L using the following expressions:

$$\bar{w} = \sqrt{\frac{L}{\rho(1/T)\int_{\text{wb}} A(t)dt}}, \tag{17}$$

$$P_{\text{ind,ideal}} = \frac{1}{2}\bar{w}L, \tag{18}$$

$$k = P_{\text{ind}}/P_{\text{ind,ideal}}. \tag{19}$$

Defining wake area for power measurements

Although our measurement area was 166×168 mm, the area affected by the animal's beating wings was considerably smaller (see Results). Therefore, we masked out the wake before calculating power and forces (average masks for the near and far wake data are shown in Fig. S3A). Masking was done in each frame using the image segmentation technique 'active contours'. The process was as follows. (1) Create a binary image where $w > 0.2$. The cut-off value did not affect the outcome to a large extent, as the image was only used as a starting point for the algorithm. (2) Create an active contour using MATLAB's image processing toolbox function activecontour with the method 'Chan-Vese', a smooth factor of 0.5 and a contraction bias of −0.2. Parameter values were chosen because they created the masks that most resembled a manually defined mask. (3) The active contour created holes in the wake as well as many small 'islands' around the measurement area, which were clearly due to noise and not actually a part of the wake. To amend this, we defined the largest island as the main wake footprint and filled the holes in this area. Additionally, islands smaller than 13 mm^2 and more than 13 mm (10 vectors) away from the main wake area were discarded.

In principle, it should not matter how the wake area is defined, as long as all vertical velocities≠0 are included. However, all PIV data include some amount of noise, which is why we attempt to mask as precisely as possible. Because there is no exact way of deciding where the wake limits are, we performed all subsequent calculations three times as follows: (1) with the mask calculated with active contours; (2) masked with a rectangle exactly fitting the previously calculated mask; and (3) with a rectangle increased by 40% in each dimension, approximately doubling the rectangle area (Fig. S3B). The two rectangular masks were only used for investigating the effect of the masking, while all other calculations were made with the mask constructed with active contours.

Defining wingbeats

Because our dataset was large enough (33,004 frames) to prevent us from being able to manually define start and stop of each wingbeat, we used an algorithmic approach. First, we calculated a component of the thrust (F_T) following Noca (1997) as:

$$F_T = \rho \iint y w \omega_z \, dS, \tag{20}$$

where y is the distance along the spanwise direction, ω_z is the in-plane vorticity and S is the wake area. Thrust is directed in opposite directions during the two half-beats, resulting in a net force of zero. This was the most cyclic variable we could find and was thus suitable for detecting the cyclic wingbeats. As the signal was often noisy, we smoothed it by removing all frequencies above approximately twice the wingbeat frequency (2×75=150) using fast Fourier transforms (fft and ifft in R). Peaks in the smoothed signal were then detected using the R function findpeaks, with a minimum peak distance of six frames (Fig. 2B). The peaks were interpreted as start and stop of a wingbeat, resulting in an average calculated wingbeat frequency of 69 Hz for all near wake sequences.

Because lift and power are calculated in each time step, and not per wingbeat, the accuracy of the wingbeat detection is not crucial to the results. The calculation of k, however, does use average data from an integer number of complete wingbeats, and so errors in detection may lead to larger variability in this parameter, but is unlikely to affect the mean substantially.

Statistics

To test whether there were any differences in wingbeat kinematics between near and far wake measurements, we performed a mixed linear model with each of the kinematic parameters as dependent variables, and included sequence nested within individual and individual as random variables and feeder position as a fixed factor. We also tested whether amplitude and frequency were correlated using a mixed linear model with amplitude as dependent variable and frequency as continuous variables and sequence (nested within individual) and individual as random variables. Feeder position was also included in the model as well as the interaction between feeder position and wingbeat frequency. We repeated the last test using stroke plane angle as a dependent variable and body angle as a continuous variable instead of amplitude and frequency. Similar analyses were performed for the PIV data as for the kinematic data. We used a mixed linear model with feeder position as a fixed factor and, as before, sequence nested within individual and individual were included as random factors. As dependent variables, we used lift, induced power or k. We further analyzed the relationship between induced power and lift using a mixed model with feeder position as a fixed factor and included the interaction between feeder position and lift. Sequence nested within individual and individual were included as random factors.

To test whether kinematics influenced the PIV-related results, we calculated sequence averages for each of the variables and used a mixed linear model with each of induced power, lift and k set as the dependent variable and each of amplitude, frequency, stroke plane angle and body angle as the continuous variable. We also included feeder position and the interaction between feeder position and the kinematic variable in the model (except when testing k, because we then ran out of degrees of freedom). Individual was used as a random variable.

We tested the predictability of Ellington's (1984b,c) model using a mixed linear model with induced power or k as the dependent variable (with predicted power from Ellington's model, using either the average weight or average lift), feeder position and power estimation method (PIV or Ellington's model) as fixed factors, and included the interaction between feeder position and power estimation method. Sequence nested within individual and individual were included as random factors.

Because we used different ways to estimate the weight of the individuals used in the Ellington model calculations, we tested whether this resulted in differences in the induced power estimate using a mixed linear model with induced power and k as dependent variables, and the weight estimate method and feeder position as fixed variables. We included the interaction between feeder position and weight estimate method. Sequence nested within individual and individual were included as random factors.

All tests, unless otherwise stated, were performed in JMP Pro 15.0.0 (SAS Institute Inc.) using the MIXED procedure with REML.

RESULTS
Kinematics

The average of the kinematic parameters wingbeat frequency (f), wingbeat amplitude (Φ), wing stroke angle (θ) and body angle (β) were relatively similar between individuals (Fig. 3A–C, Table S2). From these data, we calculated an average Reynolds number of 2000, representing hovering in these moths. Some individuals – most clearly individual M1 – varied their kinematics considerably between different sequences. In addition, moving the feeder vertically 100 mm resulted in significantly different kinematics
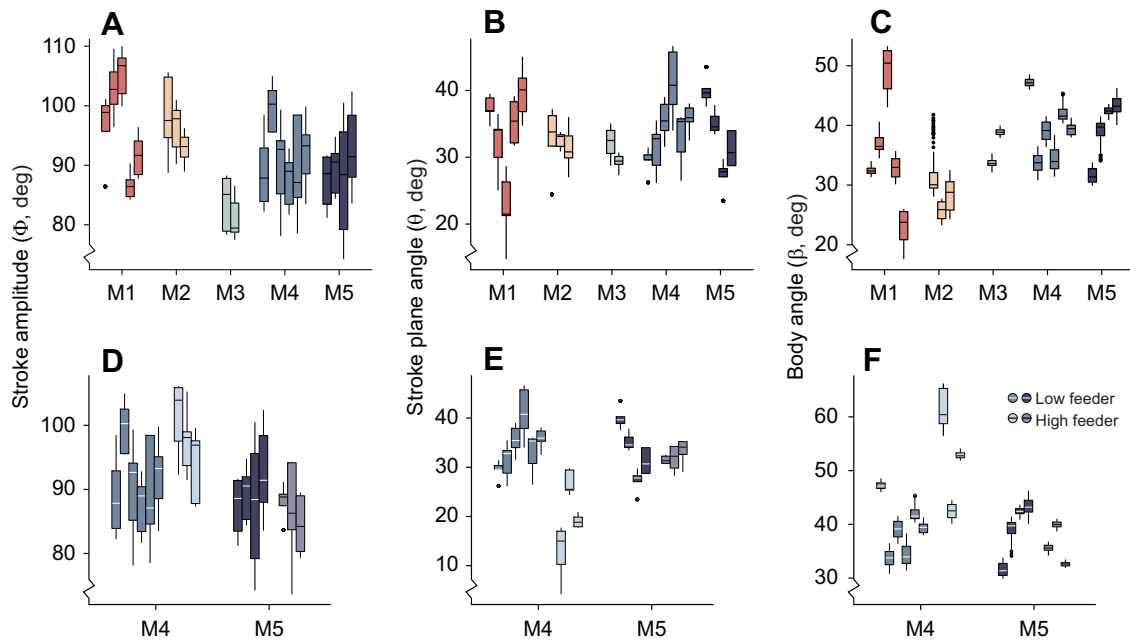
Fig. 3. Kinematics of hovering flight in *Macroglossum stellatarum*. (A) Stroke amplitude (Φ), (B) stroke plane angle (θ) and (C) body angle (β) of all individuals (M1–M5) during sequences recorded with the standard feeder placement. (D) Stroke amplitude (Φ), (E) stroke plane angle (θ) and (F) body angle (β) of two individuals during sequences recorded with the standard feeder placement (40 mm above laser sheet, 'low') as well as with the feeder placed 140 mm above the sheet ('high'). Each box represents one sequence.

(Fig. 3D,E, Table S2). We did not find any effect of feeder position on amplitude or body angle. However, there was a difference in frequency, with higher values for the high feeder position (79.3 versus 74.4 Hz, P=0.0123, d.f.=20.17), as well as for stroke plane angle, with lower values for the high feeder position (26.0 versus 33.3 deg, P=0.0118, d.f.=23.64).

We found a significant negative relationship between amplitude and frequency (Φ=154−0.79f, P<0.0001, d.f.=160.2). There was also a significant effect of the feeder position (P=0.0094, d.f.=36.24), with higher amplitude at a given frequency for the high feeder position. There was no effect of the interaction between feeder position and frequency.

It should be noted that, even though we present data for stroke plane angle (θ) and body angle (β) as though they were independent variables, the moths kept a relatively fixed angle between wing stroke and body during flight (Fig. 4). There was a negative relationship between stroke plane angle and body angle (θ=60.8−0.828β, P<0.0001, d.f.=32.44), with lower stroke plane angles for a given body angle at the high feeder position (P=0.0465, d.f.=18.09), but no effect of the interaction between body angle and feeder position.

The path of the wing tip is presented as an average for each moth in Fig. 5. Viewed from the side, the motion is similar to two C-shapes, one for each half-stroke. The downstroke is consistently located above the upstroke. The path does not follow a figure-eight pattern as in many other insect species in hovering flight.

To show how the wing moves over time, two parameters, φ and γ, are presented against normalized time (τ) in Fig. 6 and Fig. S2C, respectively. During a wingbeat, stroke angle (φ) closely followed a sinusoidal motion (Fig. S2C). Elevation angle (γ) instead displayed a slightly more complex pattern: while both half-strokes also here moved with a sinusoidal motion, the downstroke had half the wavelength of the upstroke and a considerably lower amplitude.

Wake topology

During both half-strokes, a hovering *M. stellatarum* sheds vorticity from the wing tips as well as the wing roots (Fig. 7). The root vorticity reflects a decrease in circulation over the body. The tip and root vortices are connected by starting and stopping vorticity to form one vortex ring per wing during downstroke, each encircling a downwards directed jet. During the upstroke (shown as red in Fig. 7A,B), weaker ring structures are generated, one for each wing. However, the vortex structures from the two half-strokes are not linked. While the rings produced during downstroke (shown in blue in Fig. 7A,B) are angled slightly backwards (indicative of weight support and negative thrust production), the upstroke vortex structures have an opposite, but larger, tilt, so that the induced
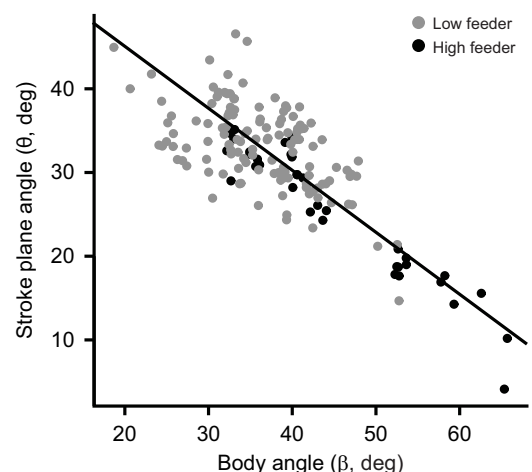

Fig. 4. The relationship between body angle (β) and stroke plane angle (θ) in all individuals and recordings. Each point represents one wingbeat, and the line is the linear regression defined by θ=60.8−0.828β.
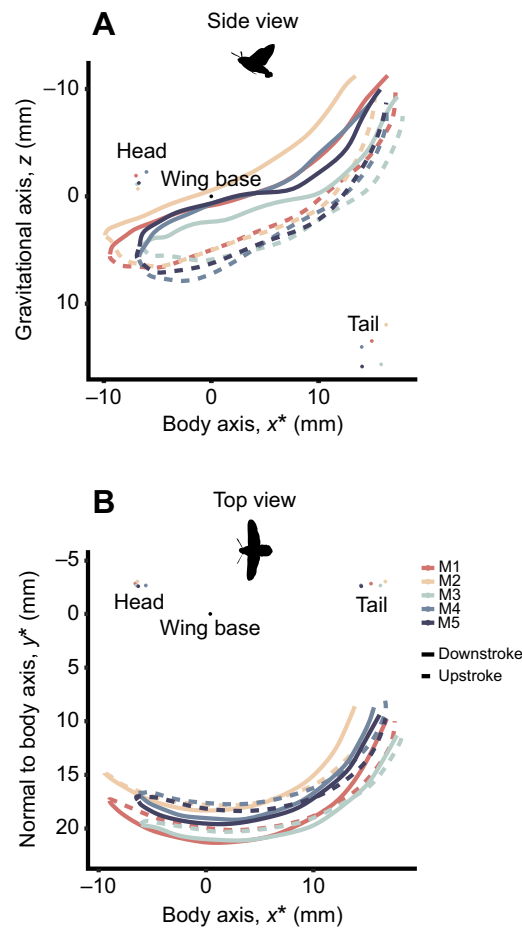
Fig. 5. Smoothing splines of the wing stroke for each individual during flights with the standard feeder placement, visualized from the side as well as from above. A rotated coordinate system, which is aligned with the body axis, is used. The origin is defined as the wing base. Asterisks indicate that the coordinate system has been rotated around the z-axis to become moth-centric.
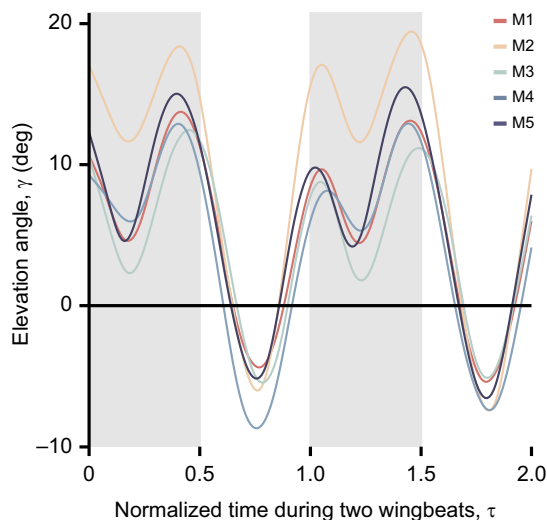

Fig. 6. Smoothing spline of each individual's elevation angle (γ) over two wingbeats. Included are all wingbeats recorded with the feeder at the default, low position. Grey area is downstroke and white area upstroke.

velocity is angled obliquely backwards as a result of thrust and some weight support being generated. The upstroke vortices are drawn out vertically, probably owing to the fact that vorticity shed in early upstroke is closer to the region of strong downwash created by the previous and subsequent downstrokes, while vorticity shed later travels downwards to the measurement plane at a lower speed. The upstroke is clearly aerodynamically active in this species during hovering, but the vortices do not appear to be of comparable strength to those produced during downstroke. Therefore, we can assume that the downstroke is the dominating contributor of weight support.

Owing to the very low speed of the wind tunnel (0.1–0.3 m s^{-1}), the wake is found directly below the animal, and travels towards the horizontal measurement plane almost solely by the self-induced convection speed of the vortices. Because the two half-strokes generate velocities of both differing magnitude and direction, the structures are prevented from moving downwards at a uniform speed, which causes the wake to appear substantially deformed when it reaches the measurement plane. This makes it impossible to determine the exact timing of shedding of vortex structures in the wake, as well as quantifying the relative contribution of the upstroke and downstroke to the overall force balance.

Occasionally we found double vortex structures associated with the upstroke between successive downstroke wake elements (Fig. 7C). We interpret this as the stop vortex of the upstroke being generated close to the strong start vortex of the subsequent downstroke, which causes it to move around the start vortex and into the downwash region of the following downstroke vortex ring (Fig. 8). The wake of the next upstroke will then be found directly above the wake of the preceding upstroke, making it appear as if there are double tip and root vortices generated by one upstroke. In addition, the start vortex of the upstroke is often found inside the downwash region of the downstroke, despite being generated above the downstroke stop vortex. This is likely a result of the upstroke vortex having a self-induced rearward motion, in combination with the flow induced by the downstroke stop vortex. As a result, there is an interaction between the downstroke and upstroke vortex rings, which we consider the cause of a deformation of the shape of the downstroke vortex ring (Fig. 7A).

In the far wake – approximately 140 mm below the animal – the deformation of the wake has become so severe that we see very few vortex structures resembling the 'near' wake (Fig. 9). There are no longer any visible vortex rings from either half-stroke, and the cross-sectional wake area is considerably larger than in the near wake measurements (Fig. 10). Vertically elongated vortices of both senses of rotation can be seen in all sequences recorded at this distance. These are likely upstroke vortices, as these could be seen as drawn out – albeit to a lesser extent – already at a distance of approximately 40 mm below the animal.

Lift

We did not find any difference in lift between the two feeder positions ($P=0.867$, d.f.$=20.4$). Neither did we find any correlation between kinematics and lift (amplitude, $P=0.75$; body angle, $P=0.68$; stroke plane, $P=0.99$; frequency, $P=0.07$), but the interactions between stroke plane and feeder position and between body angle and feeder position had a significant effect on lift ($P=0.0238$, d.f.$=14.32$, and $P=0.0197$, d.f.$=14.88$, respectively). The interaction term suggested a lower slope between lift and stroke plane angle in the high feeder position than in the low feeder position and the opposite for the body angle. Because the average lift force calculated with the far wake
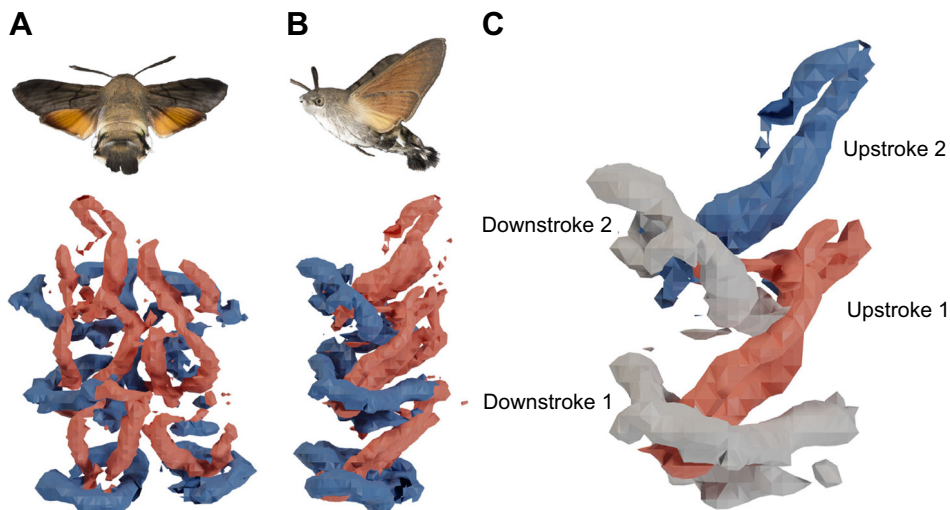
Downstroke 2

Upstroke 2

Upstroke 1

Downstroke 1

Fig. 7. The 'low feeder' wake from three wingbeats of a hovering *M. stellatarum*, visualized with iso-surfaces of constant *Q*-value. Blue shapes represent downstroke vortices and red shapes upstroke vortices (A and B). The wake from the two bottom wingbeats, only showing vortex structures from the left wing (C). The stop vortex from upstroke 1 (in red) has moved into the downwash region of the wake shed from downstroke 2. The figure is generated from 38 consecutive slices through the wake displaced based on the average downwash of speed 1.28 m s^{-1}.

equation is close to the weight (mass×*g*) of moths from the same colony (mass=0.297 g when calculated from *L*, mass=0.281 g from Warfvinge, 2019), we can be confident that we have collected data from the mature wake.

Induced power

There was a significant difference in the measured induced power between the two feeder positions (*P*<0.0001, d.f.=20,5), with lower induced power for the high feeder position (1.70 mW) compared with the low feeder position (2.50 mW). When controlling the induced power for the lift generated, we still found a significant effect of feeder position, with lower induced power for a given amount of lift at the high feeder position (*P*<0.0001, d.f.=21.76). The interaction between lift and feeder position was also significant, with a lower slope of the lift–power relationship for the high feeder position (*P*<0.0001, d.f.=2958).

Induced power measured with PIV (Eqn 15) was consistently lower than that predicted by the actuator disk model (Eqns 7, 9). Fig. 11A shows violin plots of all data for each individual along with P_{ind} calculated with the actuator disk model, using the highest and lowest values of *k* found in the literature (*k*=1.2: e.g. Willmott and Ellington, 1997; k_{span}=2.17: Henningsson and Bomphrey, 2013). In addition, P_{ind} measured farther down in the wake (black 'violins') was somewhat lower than the measurements from the default feeder placement (grey). The 'violins' (geom_violin in R, with a Gaussian kernel and default settings) display the kernel density of the data, i.e. the width of each shape represents the probability of finding data at this *y*-value.

Induced power calculated with Ellington's model (Eqns 10–14) yields significantly higher values than both the PIV data and the classic actuator disk model (Fig. 11B). When comparing the induced power estimated from the PIV measurements (2.10 or 2.26 mW) with that of Ellington's model, we found significant differences between estimates, using both average weight (6.97 mW, *P*<0.0001, d.f.=3130) and average lift (6.34 mW, *P*<0.0001, d.f.=3128) in Ellington's model, with lower values from the PIV measurements. In addition, we found a significant effect of the interaction term between power estimate method (PIV or Ellington) and feeder position (*P*<0.0001, d.f.=3130, and *P*<0.001, d.f.=3128, respectively), suggesting that the difference in induced power estimate for the feeder positions differed more for the PIV measurements than for the Ellington model estimates. Interestingly, the data collected during the far wake experiments

(black) result in a lower induced power for Ellington's model, even though the model is based purely on kinematics. It is therefore possible that the corresponding differences observed in the PIV data can be explained by kinematic differences (see above) and are not only affected by how far down in the wake the measurements are made. However, kinematic differences between individuals in the modelled dataset (Figs 5 and 6) result in almost no between-individual differences in measured induced power output (Fig. 11A). The only kinematic factor that had an effect on measured induced power was frequency, with higher frequency being related to higher induced power (P_{ind}=−0.002538+5.8 10^{-5}*f*, *P*=0.0483, d.f.=14.17). None of the other kinematic parameters had a significant effect (amplitude, *P*=0.82; body angle, *P*=0.55; stroke plane angle, *P*=0.29), nor did any of the interactions between the kinematic variables and feeder position.

While the plot of the PIV data (Fig. 11A) shows one violin shape representing all data for each moth, the plot showing Ellington's model (Fig. 11B) splits each shape into two halves. This is to show the result calculated with the two different estimations of body weight. Although there are sometimes large discrepancies between the data calculated with the two different weight values (especially in M3), both estimates result in the same trend: a relatively higher P_{ind} when using Ellington's model compared with using PIV data, with a reduced variation when calculations are based on far wake sequences. However, the different weight estimate methods generated significantly different induced power estimates (*P*<0.0001, d.f.=304), and also differed in how they responded to the changes associated with the feeder placement (*P*<0.0001, d.f.=304).

Induced power factor (*k*)

We did not find a significant difference in *k* between the feeder positions (*P*=0.10, d.f.=23.8). The intercept in the model was estimated to *k*=1.42. Similar to the P_{ind} measurements, *k* was estimated to a lower value with PIV than with Ellington's model (Fig. 11C,D), using both average weight (*P*<0.0001, d.f.=3132) and average lift (*P*<0.0001, d.f.=3131) for the model predictions. However, the difference between measurements and model calculations was less pronounced for *k* than for P_{ind}. The average PIV-based values of *k* were 1.42 and 1.43 when using body weight and lift force, respectively, while the model estimated *k* to 1.64 and 1.61 (Table S1). There was also a significant interaction between method and feeder position when using average lift in Ellington's
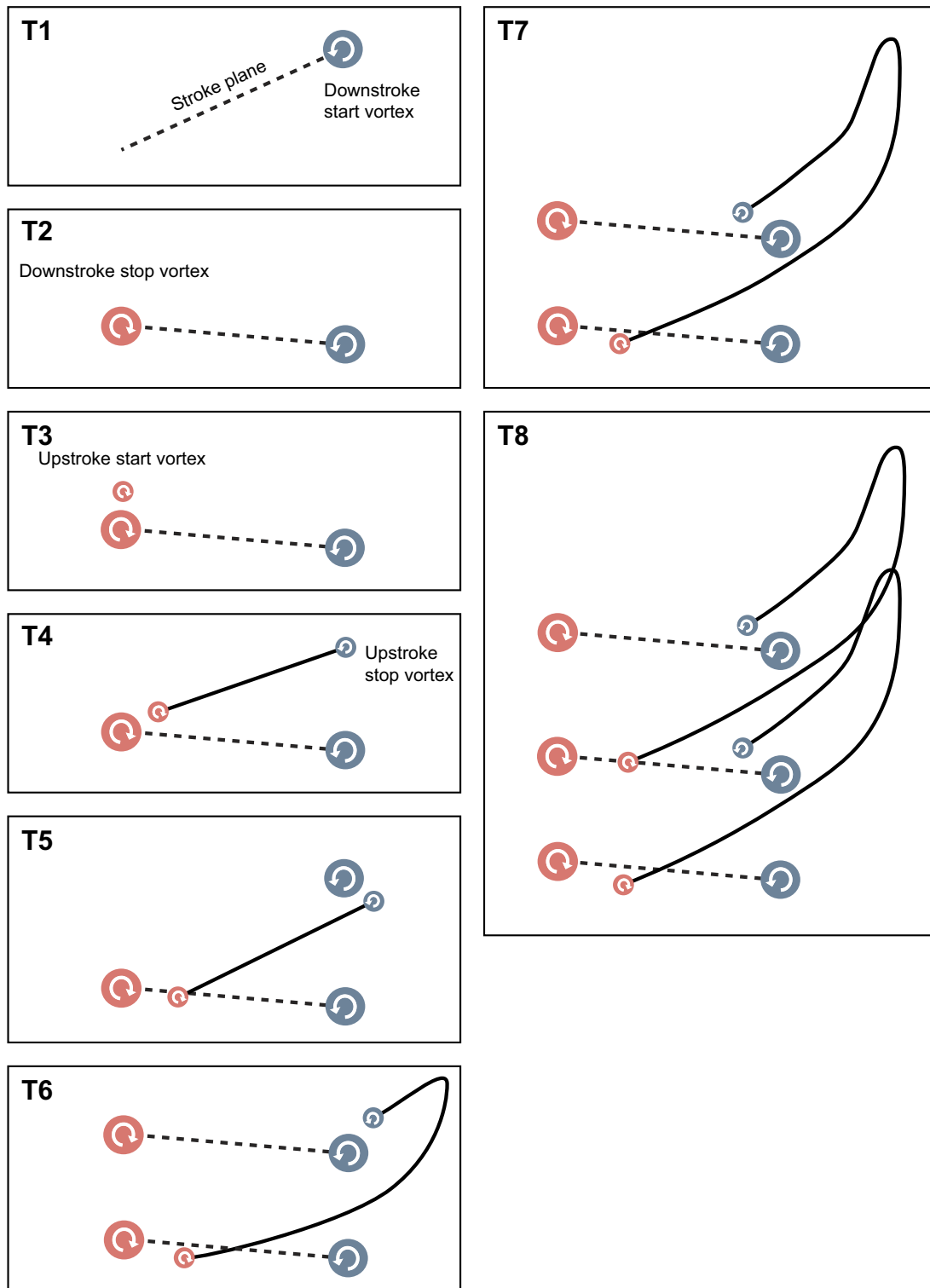
Fig. 8. Our interpretation of how the double upstroke vortex structures are generated, as seen from the side, shown in eight time steps (T1–T8).

model ($P<0.0001$, d.f.=3131), but not when using average weight ($P=0.3539$, d.f.=3132).

There were two kinematic factors that had a significant influence on k – stroke plan angle ($k=1.16+9.5\times10^3\theta$, $P=0.0018$, d.f.=18.92) and body angle ($k=1.67-6.3\times10^{-3}\beta$, $P=0.0128$, d.f.=18.62) – whereas frequency ($P=0.2608$) and amplitude ($P=0.1432$) did not have significant effects. Because the two variables, stroke plane

angle and body angle, are highly negatively correlated and functionally interlinked, the two results represent the same thing.

Evaluating the definition of wake area

Wake measurements of P_{ind} were not affected by whether the regular calculated wake area was used or whether it was expanded to a tightly fitted rectangle (Fig. S4). Even an area almost double the size of this
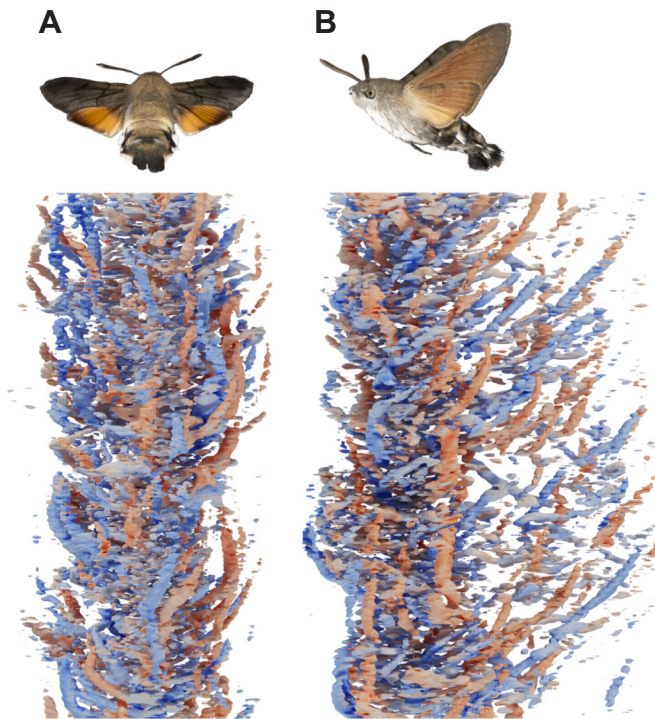
Fig. 9. The 'high feeder' wake from an unknown number of wingbeats of a hovering *M. stellatarum*, visualized with iso-surfaces of constant *Q*-value and coloured by *z*-vorticity. (A) Rear view. (B) Side view.

rectangle did not affect the values significantly (*t*-test between P_{ind} with smallest and largest area: P=0.61, t=−0.51, d.f.=4523.7). However, estimations of *k* were, as expected, severely affected by choice of area: a tightly fitted rectangle produced a *k* value 35% higher, while the enlarged rectangle caused a 78% increase (*t*-test between smallest and largest area: P<2.2×10⁻¹⁶, t=−123.7, d.f.=3721.5).

DISCUSSION
Wake topology
Experimental and simulated work from recent years has shown that the vortex wakes of flying animals are often more complex and difficult to interpret than any previously imagined model (see e.g. Hedenström et al., 2007; Håkansson et al., 2015; Henningsson et al., 2015; Johansson et al., 2016, 2018). This is also the case for the wake of hovering *M. stellatarum*. However, the wake could be

conceptually simplified as consisting of pairs of vortex rings – one per wing – shed during each half-stroke (in support of model E in Fig. 1). This is similar to the wake structure previously predicted by both flapper (van den Berg and Ellington, 1997) and CFD studies (Aono et al., 2009) for the larger *M. sexta*. However, an inclined stroke plane angle has previously been associated with a wake consisting of only downstroke vortex rings (Ellington, 1984b), and the stroke plane angle of *M. stellatarum* (as well as *M. sexta*) lies well above the cut-off angle (∼33>20 deg) for when an inactive upstroke is considered likely (Fig. 1D). It could be argued that the dichotomy between 'normal' and 'inclined stroke plane' hovering is unnecessary because stroke plane angle is a continuously varying parameter. Perhaps it would be more useful if the angle itself could be used to predict the contributions of the upstrokes and downstrokes to the force balance. We suggest that future studies should make an effort to link kinematics and wake to specific wingbeats in order to estimate the effect of stroke plane on relative force contribution between downstrokes and upstrokes.

The vortex rings shed during downstroke and upstroke are unlinked (i.e. have separated vortex cores), with separate start and stop vortices, in contrast to what has been concluded based on previous dust-flow visualization (Brodsky, 1994), a mechanical flapper (van den Berg and Ellington, 1997) and recent schlieren photography (Liu et al., 2018), which all show linked downstroke and upstroke rings similar to Fig. 1F. Coupled vortex rings, or a 'ladder' structure, can be an indication of the wing capturing the wake from the previous half-stroke, i.e. the wing interacts with the flow generated by the previous half-stroke in such a way that only a single vortex structure is generated at the transition between half strokes. As we see no signs of this in our data, it is possible that *M. stellatarum* employs a less efficient wing stroke than the larger *M. sexta*. Alternatively, the previously applied techniques may have been unable to separate the start and stop vortices from the downstroke and upstroke because they occur in close proximity to each other, particularly in the near wake. However, in *M. stellatarum* it is clear that the start and stop vortices from the downstroke and upstroke are distinct structures already when shed from the wing, as observed from near wing measurements (Johansson et al., 2013).

Although the moth may not be able to take advantage of its previously shed wake, it is clear that wake elements interact between consecutive strokes, which deforms the wake so that it is difficult to pinpoint the origin of the different vortex elements. This is mainly due to the non-uniform downwash, which causes the different wake structures to travel downwards at varying speeds. As a result, the time and space variables of our data are confounded, and we cannot,
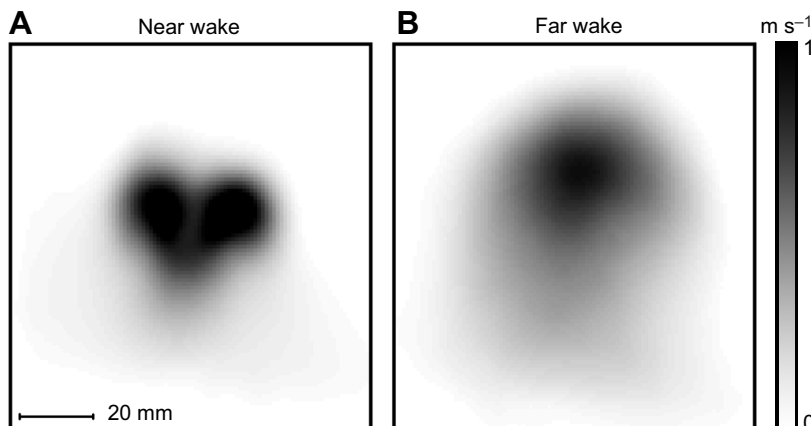

Fig. 10. Average downwash of all flight sequences, for all individuals, in the near and far wake experiments. The image plane is seen from above, with the moth directed towards the top of the image.
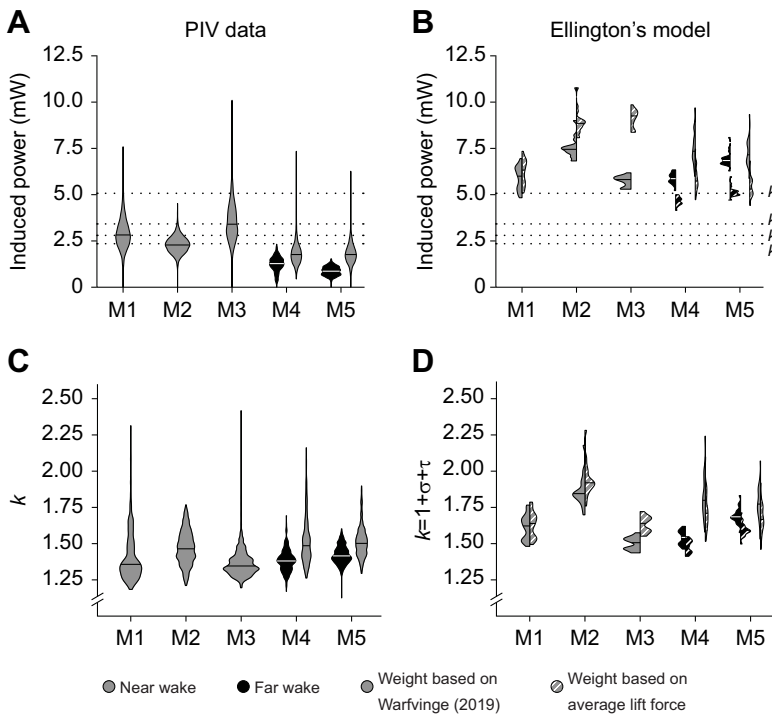
Fig. 11. Aerodynamic properties as derived on the basis wake measurements and a model. (A,B) Induced power measured with particle image velocimetry (PIV; A, Eqn 15) as well as estimated with Ellington's model (B). Means are displayed as a line through the 'violin' shapes. In the dataset used when creating the shapes (which represent the kernel density of the data), one frame equals one data point. Dotted lines are Pennycuick's version of the actuator disk model with the highest and lowest k found in the literature (k=1.2, e.g. Willmott and Ellington, 1997; k_{span}=2.17, Henningsson and Bomphrey, 2013) along with k=0 and k calculated from the PIV data (1.45). (C,D) Kernel density estimates of k measured with PIV (C, Eqn 15) as well as estimated with Ellington's model (k=1+τ+σ; D). One wingbeat is one data point.

with certainty, determine the timing of vortex shedding. This is illustrated by the double upstroke vortices sometimes visible in the wake. We interpret this as a result of the influence of the downstroke vortex ring on the subsequent upstroke ring. An alternative interpretation could be that the wing in fact sometimes releases two tip vortices during the upstroke. Such an extra vortex was recently observed in the wake of near-hovering *M. sexta* and was suggested to originate from the tip of the hindwing (Liu et al., 2018). However, we do not find this interpretation plausible for *M. stellatarum*, as our specimens had tightly coupled wings, unlike the *M. sexta* of Liu et al. (2018), which had visible gaps between the forewings and hindwings. In addition, the two vortices in *M. stellatarum* were found at the same distance from the body, which would not be expected if one was shed from the much shorter hindwing.

Wake evolution

We could identify three main patterns of the evolution of the wake. First, as the vortices travel downwards after leaving the wings and body, the wake structures become increasingly difficult to interpret, eventually appearing almost chaotic in character. In the far wake, it is often difficult to discern any periodicity related to wingbeat frequency. A similar effect was found by Cheng et al. (2014) in a study using a robotic flapper with a *Drosophila* wing shape but a Reynolds number similar to that of a hawkmoth. Here, no distinct vortex structures were found after approximately three-quarters of a wing length below the wing. As a comparison, our near-wake data – which do have distinct structures – were recorded at a distance of approximately two wing lengths (or five chord lengths) below the animal, while the far-wake data were recorded seven wing lengths (or 18 chord lengths) below. In a study investigating vortex interactions with a pitching and heaving mechanical wing, Lentink et al. (2010) predicted that animals flying slower than a certain relative velocity (see their paper for details about how the velocity is calculated) could experience near-chaotic wake interactions. Recorded during hovering, our data are well below the suggested

velocity threshold, and thus the chaotic nature of *M. stellatarum* wakes corroborates the authors' suggestion. One implication is that wakes of slowly flying animals should be recorded as close to the flier as experimental restrictions allow, but our variation in kinematics within sequences also suggests that determining whether the wake is truly chaotic requires a more detailed analysis.

Second, vortices released during upstrokes are vertically elongated, appearing to stretch over the wakes of multiple wingbeats. At two wing lengths below the animal, upstrokes are already visibly stretched out. We have attributed this to the fact that the beginning of the upstroke is closer to the preceding downstroke than the end of upstroke, and so is more affected by its downwash. Evidently, the effect is exacerbated over time. To resolve this issue, we would suggest capturing a volume of the wake large enough to capture a full wingbeat, as close to the animal as possible.

Third, upon reaching the far wake measurement plane, the whole wake has become stretched out in the wind tunnel flow direction (*x*-axis), supporting the notion that the downstroke and upstroke wakes move in different directions owing to the thrust/negative thrust generation. This is visualized in Fig. 10 showing the average downwash of the near and far wake measurements. Here, it is clear that the cross-sectional area of the wake is larger further away from the animal, contrary to the theoretical expectation of a contracting wake (Ellington, 1984c). This has consequences for estimations of flight efficiency. In a study of a robotic flapper designed to resemble a *Drosophila*, but with a Reynolds number corresponding to a large hawkmoth in cruising flight (*Re*=2200), Cheng et al. (2014) showed that the flapper's wake expanded in the flow direction, while contracting in the span direction. However, we did not observe a spanwise contraction; instead, if anything, the width of the wake was slightly increased in the span direction. This could indicate generation of side forces, which are suggested to be used for manoeuvring/positioning. In addition to causing the wake to move in directions other than vertically downwards, thrust and sideways forces generate a vortex ring tilted relative to the horizon, which, owing to the relatively low self-induced velocities, will cause the

wake to appear larger than it is when it reaches the measurement plane (the same mechanism as described for slow speed flight measurements in birds; Johansson et al., 2018). Although we observed a larger cross-sectional area for the far wake, there is no evidence for the prediction of two separating vortex rings posited by van den Berg and Ellington (1997) and Aono et al. (2009). Rather than a larger region of low flow beneath the body, indicative of separating rings, the average downwash of our far wakes is strongest in the centre (Fig. 10). This could be an indication of merging vortex rings – a possibility suggested by Liu and Aono (2009) to be related to higher Reynolds numbers. In addition, complicating factors, owing to the low Re viscous flow, such as entrainment as the wake moves downwards, may result in an increase in the wake size, while speed is reduced (Shinde and Arakeri, 2018). Determining whether this latter mechanism is a real concern will require future studies capable of tracking the evolution of the wake structures over time.

Kinematics

The aims with the kinematic measurements of this study were threefold. Firstly, the kinematics serve as an input into aerodynamic power models, which are evaluated below. Secondly, we wished to investigate possible links between variations in kinematic parameters and wake topology. That we did not succeed in the latter endeavour is likely due to a combination of several factors, one being that we had no way to directly connect individual wingbeats between kinematic and wake data. This is due to the fact that the wake travels towards the measurement plane for an undetermined period of time, and so the two datasets do not represent the exact same set of wingbeats, even though the measurements are perfectly synchronized in time. If the transition time were always the same, a constant shift would suffice to synchronize the measurements. This was not the case, and perhaps a more interesting reason for the inability to link kinematics to the wake is the possibility that small variations in kinematics result in large and unpredictable effects in the wake owing to wake interactions. For example, kinematic variations between wingbeats can cause wake structures of successive wingbeats to collide, owing to different convection velocities. Thirdly, we wanted to test whether any of the kinematic variables predicted the measured induced power or influenced k. The only kinematic parameter with an impact on induced power was wingbeat frequency, where a higher frequency increased P_{ind}. Based on Eqns 12 and 13, we expect the effect of wingbeat frequency to be twofold, affecting the wingtip velocity in Eqn 12 and f_v in Eqn 13. A higher f_v should reduce τ and hence k and P_{ind}. An increased wingtip velocity will reduce σ in Eqn 12 and likewise cause a reduction of P_{ind}. The result was thus contrary to expectations, which could indicate that an increase in frequency is associated with some other kinematic change (e.g. angle of attack) that we have not measured that, in turn, results in increased induced power. The kinematic effect on k was restricted to stroke plane (and the correlated body angle), where a higher stroke plane angle resulted in a higher k. This is in line with expectations given that a higher stroke plane angle will result in a smaller A_0 and hence a higher τ. From these results, we would argue that some of the basic assumptions regarding kinematic influence on power requirements in Ellington's model are valid.

The wing tip path of hovering *M. stellatarum* may look relatively simple (Fig. 5), but when studying the elevation angle of the wing stroke (Fig. 6) an interesting pattern appears. Instead of two mirrored half-strokes, together forming a figure-eight or an oval shape, the half-strokes follow two different patterns.

While the downstroke traces half of a figure-eight, the upstroke wing tip moves in the shape of a half oval. Sane and Dickinson (2001) investigated the effects of wing tip path on, among other things, flight forces, and found that although a figure-eight path created higher force peaks, both path types produced average forces of similar magnitude. For *M. stellatarum*, both half-strokes start with a downward motion, which Sane and Dickinson (2001) suggested contributes to a higher degree of wake capture (Dickinson et al., 1999), owing to the wing moving towards the wake from the preceding wingbeat.

From our results, it is clear that the upstroke is to some degree aerodynamically active in *M. stellatarum*, despite the use of an inclined stroke plane. Ellington's model assumes either an equal contribution of the upstroke and downstroke or an inactive upstroke. Recent modelling by Vejdani et al. (2018) further supports this notion: they found that animals that cannot retract their wings, such as insects, are better off using a horizontal stroke plane and equal contribution of the downstroke and upstroke to the lift production than using an inclined stroke plane. However, as pointed out by Vejdani et al. (2018), the torques of the wing forces on the body also need to balance in order to hover stably, and it may well be that the use of an active upstroke in *M. stellatarum* is a result of a need to manoeuvre properly. This notion is supported by the cyclic behaviour of the thrust production that we found, which is only wasteful from a power perspective.

Does hovering require extra effort?

One of the persevering questions regarding hovering flight in insects is whether hovering is more costly than forward flight (Ellington et al., 1990). In the present study, we measured induced power only in hovering *M. stellatarum*, but in a previous study, we measured power expended during forward flight (1.5 m s^{-1}) in the same species (Warfvinge, 2019). This speed has been suggested to be the preferred flight speed of the species (Henningsson and Bomphrey, 2013). Comparing the average power values in these two studies [hovering: 2.50 mW (low feeder value), forward flight: 1.51 mW], it is clear that hovering requires substantially more power than flying forward at 1.5 m s^{-1}. It is worth noting that the value for forward flight is the total power (including parasite and profile power), while the power from the present study is the induced power only. This makes a direct comparison difficult. However, because induced power is a subset (although dominating during hovering) of total power required, the true difference in flight effort is likely even larger than this comparison indicates. This conclusion is in line with a recent study (Warfvinge et al., 2017) showing that the large hawkmoth *M. sexta* requires more power when flying at slow (1 m s^{-1}) and fast (4 m s^{-1}) speeds than at intermediate speeds (2–3 m s^{-1}). Taken together, our results thus support the notion of costly hovering in insects, or at least moths.

Is Ellington's model useful?

Induced power calculated with Ellington's (1984b) model for hovering insect flight consistently produced higher values than induced power measured in the wake (average from wake measurements: P_{ind}=2.1 or 2.27 mW; Ellington's model: P_{ind}=6.97 or 6.34 mW). This means that at least one of the methods produces erroneous results, but, as we will justify below, it is likely that our estimations of induced power from the wake are reasonable. If k is set to unity, Ellington's model should produce the minimum amount of induced power required to keep an insect with the specified wingspan and mass aloft. However, doing this results in a P_{ind} of 3.94 mW – still higher than our measured values. A

possible explanation for this discrepancy is the fact that the cross-sectional wake area does not contract as prescribed in the models. Instead, it seems to be the case that the wake of hovering *M. stellatarum* expands when travelling downwards towards our measurement plane(s). In the present study, the average cross-sectional wake area in the mature wake was 1.3 times larger than a circle with the diameter of the moths' wingspans (the actuator disk as defined in Pennycuick's model). This could possibly be explained by the effect seen by Cheng et al. (2014). Compared with the disk defined in Ellington's model, the wake area was 3.8 times larger. Therefore, we find it unlikely that this large discrepancy is merely due to a wake expansion in one dimension only. However, comparisons between the PIV data of the near wake with those of the far wake show that the average area of the latter was 3.7 times larger than the former. This supports the notion of an expanding (potentially owing to viscous entrainment) or diverging wake (owing to thrust and side forces generated), but the number itself may be inflated by larger uncertainties to define the wake area in the far wake measurements owing to fuzzier wake structures. In his original paper on the vortex theory of hovering flight, Ellington (1984c) had already indicated that experimental tests, such as those presented here, of the wake topology and area are critical to evaluate the validity of the assumptions of the model. Of vital importance is the experimental test of the definition of the disc area, which, according to our results, expands rather than contracts. The reason for this is not clear at the moment, but is likely due to the fact that shedding of vortex sheets deviates from the horizontal, as suggested by our wake visualizations. As a result, there will be horizontal velocities induced to the wake that cause spreading and wake expansion.

In summary, neither Ellington's model in its present form nor the actuator disk model seem suitable for predicting aerodynamic power in small, hovering hawkmoths. The assumption of a contracting wake adds a factor of 4 to the induced power equation when using the version defined for the disk (Eqn 7) instead of that of the mature wake (Eqn 8). This, if incorrect, of course has consequences for the predictions of power required in hovering flight. It may, however, be less of a problem in fast forward flight, as profile and parasite power are the dominating power components at higher speeds.

A complicating aspect of Ellington's model is the somewhat arbitrary choice between one or two pairs of vortices produced by each wingbeat. In Eqn 13, it is clear that an incorrect choice can again lead to an error of a factor of 4 in the calculation of the temporal correction factor τ. We have defined the flight of *M. stellatarum* as inclined stroke plane hovering, as the stroke plane angle averaged 33 deg (the threshold is set to around 20 deg in Ellington, 1984b). This leads to the assumption of a wake structure consisting of one pair of vortices generated by each wingbeat. The visualizations of the wake shows that the upstroke is not completely aerodynamically inactive. However, it is not clear how much the relatively weak upstroke vortices affect the induced power, as it is not possible to completely untangle the influences from the downstroke and upstroke owing to the complicated wake structures.

From our results, it is clear that the simplified model of Ellington, as perhaps expected, does not fully capture the complexity of the wakes of real insects. This may be due to, as pointed out above, an 'on/off' treatment of the upstroke, for example; however, as pointed out by Shinde and Arakeri (2018), it may also be the case that the assumptions of the actuator disc model as a pressure pump working in a single plane are not be met by the animals. The consequences of

this latter proposition, that the pressure gradient is spatially more drawn out, is currently not clear and need further exploration, which may result in a novel 'actuator slab model'.

Estimating *k*

As has been shown, the way of estimating *k* by comparing the actual velocity distribution with the ideal uniform velocity distribution is highly dependent on the (sometimes arbitrary) wake definition. A similar method that has been used repeatedly by other authors compares velocities along a line between the tip vortices with the ideal uniform velocity distribution. Here, we encountered similar difficulties in determining where the wake ends as in other studies. While some authors draw the line between the centre of the tip vortices (where the downwash speed should be zero) (Muijres et al., 2011, 2012a), others extend the measurements to beyond the vortices, for the purpose of also including the upwash created by the wings (Henningsson and Bomphrey, 2012, 2013). In our measurements, upwash (relative to still air) was not included in the original mask, as we used a cut-off value of *w* and not |*w*| to define the starting area for our masking procedure. However, most upwards-directed velocities are captured in the rectangular masks. We have no opinion on which is the correct method of estimating *k*, and so we caution against using any values calculated in this paper as definite. However, we consider it is more likely that we have underestimated the wake area than overestimated it, and so the values shown in Fig. S4 are possibly in the lower range of their true values. Hence, we find it unlikely that *k* in insect hovering flight is as low as the default value of 1.2 (used in e.g. Wakeling and Ellington, 1997; Willmott and Ellington, 1997). In addition, the values calculated with Ellington's model support the notion of a relatively high *k* in *M. stellatarum*. This is unsurprising, as Ellington (1984b), found that species with an inclined stroke plane angle had a considerably higher *k* than species performing normal hovering. This is mainly due to the choice of the factor f_v as 1 or 2 in Eqn 13. One suggestion would be to introduce an additional factor that reflects the relative contributions of the upstroke and downstroke, as a way to compensate for the integer behaviour of f_v (e.g. allowing f_v to effectively take a value of 1.4 would halve τ compared with when f_v is 1).

Near and far wake measurements

According to the principles of wake evolution prescribed by the actuator disk model, the wake contracts until it (asymptotically) reaches an area half the size of the disk area. This means that it should not matter how far down in the wake one places the measurement plane, as long as the measured wake has had time to contract sufficiently. However, we found that this is not a realistic representation of the wake below a hovering hawkmoth, as the wake area instead increases farther down in the wake (see Fig. S3A).

By measuring induced power both in the near and far wake, we show that induced power estimated from downwards velocities in the wake decreases when the measurement plane is placed farther away from the animal. Although we have no conclusive explanation for this phenomenon, it is likely that dissipation may play a role in decreasing the kinetic energy in the wake. In addition, it is unclear whether the induced power estimations are affected by the loss of structure in the far wake.

In conclusion, the modified actuator disk method we used to estimate induced power seems somewhat sensitive to properties of wake evolution. With no knowledge of how far down in the wake the vortex structures disintegrate – and whether this affects induced

power estimations – it is difficult to determine the optimal placement of the measurement plane. However, comparison of the flying animal's mass to lift force estimated using the same velocity fields can be used to retroactively evaluate the choice.

Concluding remarks

The wake of hovering hummingbird hawkmoths showed a more complex topology than any of the hypothetical wakes of Fig. 1 prescribed to apply to hovering animals. This complexity arises partly because wake elements originating as a result of the downstrokes and upstrokes warp and interact owing to differential self-convection speeds. However, when imaged relatively close under the animal, the wake shows most resemblance to a mixture of models E and F in Fig. 1. However, when imaged further away from the animal, the wake disintegrates so much that the original topology is no longer discernible. Wake vortices should reflect the magnitude and time history of the aerodynamic forces, but our experiments show that due to the differential translocation of wake elements it was not possible to determine the relative contributions of downstroke and upstroke. Resolving the relative contributions of the downstroke and upstroke will most likely require measurements around the animal itself or experimentally validated CFD models of the complete animal. However, as CFD modelling of aerodynamics of insect flight improves, the visualization of wakes in real animals remains valuable data for comparison with the CFD results.

We estimated induced power (P_{ind}) with the purpose of evaluating Ellington's (1984a,b,c) model of power required for hovering in insects. We found that the model overestimates induced power when applied to hawkmoths, and possibly other species with inclined stroke planes. Reducing the continuously variable stroke plane angle to a binary choice between horizontal (normal hovering) and inclined has a large effect on predicted power output, and this makes it difficult to recommend using this model unless the topology of the wake is known and the upstroke is either completely inactive or similar in strength to the downstroke. Alternatively, a revision of the model that takes the relative contribution of the upstroke to downstroke into account is needed. In addition, we found that hovering is a more energy-demanding flight mode than forward flight in these small hawkmoths, in contrast to what has previously been considered to apply for insect flight.

References
Altshuler, D. L., Princevac, M., Pan, H. and Lozano, J. (2009). Wake patterns of the wings and tail of hovering hummingbirds. *Exp. Fluids* **46**, 835-846. doi:10.1007/s00348-008-0602-5

Aono, H., Shyy, W. and Liu, H. (2009). Near wake vortex dynamics of a hovering hawkmoth. *Acta Mech. Sin.* **25**, 23-36. doi:10.1007/s10409-008-0210-x

Bomphrey, R. J. (2012). Advances in animal flight aerodynamics through flow measurement. *Evol. Biol.* **39**, 1-11. doi:10.1007/s11692-011-9134-7

Brodsky, A. K. (1994). *The Evolution of Insect Flight*. Oxford: Oxford University Press.

Cheng, X. and Sun, M. (2016). Wing-kinematics measurement and aerodynamics in a small insect in hovering flight. *Sci. Rep.* **6**, 25706. doi:10.1038/srep25706

Cheng, B., Roll, J., Liu, Y., Troolin, D. R. and Deng, X. (2014). Three-dimensional vortex wake structure of flapping wings in hovering flight. *J. R. Soc. Interface* **11**, 20130984. doi:10.1098/rsif.2013.0984

Dickinson, M. H., Lehmann, F.-O. and Sane, S. P. (1999). Wing rotation and the aerodynamic basis of insect flight. *Science* **284**, 1954-1960. doi:10.1126/science.284.5422.1954

Ellington, C. P. (1984a). The Aerodynamics of Hovering insect flight. III. Kinematics. *Philos. Trans. R. Soc. B Biol. Sci.* **305**, 41-78. doi:10.1098/rstb.1984.0051

Ellington, C. P. (1984b). The aerodynamics of hovering insect flight. VI. Lift and power requirements. *Philos. Trans. R. Soc. B Biol. Sci.* **305**, 145-181. doi:10.1098/rstb.1984.0054

Ellington, C. P. (1984c). The aerodynamics of hovering insect flight. V. A vortex theory. *Philos. Trans. R. Soc. B Biol. Sci.* **305**, 115-144. doi:10.1098/rstb.1984.0053

Ellington, C. P., Machin, K. E. and Casey, T. M. (1990). Oxygen consumption of bumblebees in forward flight. *Nature* **347**, 472-473. doi:10.1038/347472a0

Engel, S., Bowlin, M. S. and Hedenström, A. (2010). The role of wind-tunnel studies in integrative research on migration biology. *Integr. Comp. Biol.* **50**, 323-335. doi:10.1093/icb/icq063

Fry, S. N., Sayaman, R. and Dickinson, M. H. (2005). The aerodynamics of hovering flight in *Drosophila*. *J. Exp. Biol.* **208**, 2303-2318. doi:10.1242/jeb.01612

Gessow, A. and Myers, G. (1952). *Aerodynamics of the Helicopter*. New York: Frederick Ungar Publishing.

Grodnitsky, D. L. and Morozov, P. P. (1993). Vortex formation during tethered flight of functionally and morphologically two-winged insects, including evolutionary considerations on insect flight. *J. Exp. Biol.* **182**, 11-40. doi:10.1242/jeb.182.1.11

Håkansson, J., Hedenström, A., Winter, Y. and Johansson, L. C. (2015). The wake of hovering flight in bats. *J. R. Soc. Interface* **12**, 20150357. doi:10.1098/rsif.2015.0357

Hedenström, A., Johansson, L. C., Wolf, M., von Busse, R., Winter, Y. and Spedding, G. R. (2007). Bat flight generates complex aerodynamic tracks. *Science* **316**, 894-897. doi:10.1126/science.1142281

Henningsson, P. and Bomphrey, R. J. (2012). Time-varying span efficiency through the wingbeat of desert locusts. *J. R. Soc. Interface* **9**, 1177-1186. doi:10.1098/rsif.2011.0749

Henningsson, P. and Bomphrey, R. J. (2013). Span efficiency in hawkmoths. *J. R. Soc. Interface* **10**, 20130099. doi:10.1098/rsif.2013.0099

Henningsson, P., Michaelis, D., Nakata, T., Schanz, D., Geisler, R., Schröder, A. and Bomphrey, R. J. (2015). The complex aerodynamic footprint of desert locusts revealed by large-volume tomographic particle image velocimetry. *J. R. Soc. Interface* **12**, 20150119. doi:10.1098/rsif.2015.0119

Ingersoll, R. and Lentink, D. (2018). How the hummingbird wingbeat is tuned for efficient hovering. *J. Exp. Biol.* **221**, jeb178228. doi:10.1242/jeb.178228

Johansson, L. C., Engel, S., Kelber, A., Heerenbrink, M. K. and Hedenström, A. (2013). Multiple leading edge vortices of unexpected strength in freely flying hawkmoth. *Sci. Rep.* **3**, 3264. doi:10.1038/srep03264

Johansson, L. C., Håkansson, J., Jakobsen, L. and Hedenström, A. (2016). Ear-body lift and a novel thrust generating mechanism revealed by the complex wake of brown long-eared bats (*Plecotus auritus*). *Sci. Rep.* **6**, 24886. doi:10.1038/srep24886

Johansson, L. C., Maeda, M., Henningsson, P. and Hedenström, A. (2018). Mechanical power curve measured in the wake of pied flycatchers indicates modulation of parasite power across flight speeds. *J. R. Soc. Interface* **15**, 20170814. doi:10.1098/rsif.2017.0814

Kolář, V. (2007). Vortex identification: new requirements and limitations. *Int. J. Heat Fluid Flow* **28**, 638-652. doi:10.1016/j.ijheatfluidflow.2007.03.004

Lentink, D., Van Heijst, G. F., Muijres, F. T. and Van Leeuwen, J. L. (2010). Vortex interactions with flapping wings and fins can be unpredictable. *Biol. Lett.* **6**, 394-397. doi:10.1098/rsbl.2009.0806

Liu, H. and Aono, H. (2009). Size effects on insect hovering aerodynamics: an integrated computational study. *Bioinspir. Biomim.* **4**, 015002. doi:10.1088/1748-3182/4/1/015002

Liu, Y., Roll, J., Van Kooten, S. and Deng, X. (2018). Schlieren photography on freely flying hawkmoth. *Biol. Lett.* **14**, 20180198. doi:10.1098/rsbl.2018.0198

Muijres, F. T., Spedding, G. R., Winter, Y. and Hedenström, A. (2011). Actuator disk model and span efficiency of flapping flight in bats based on time-resolved PIV measurements. *Exp. Fluids* **51**, 511-525. doi:10.1007/s00348-011-1067-5

Muijres, F. T., Bowlin, M. S., Johansson, L. C. and Hedenström, A. (2012a). Vortex wake, downwash distribution, aerodynamic performance and wingbeat kinematics in slow-flying pied flycatchers. *J. R. Soc. Interface* **9**, 292-303. doi:10.1098/rsif.2011.0238

Muijres, F. T., Johansson, L. C. and Hedenström, A. (2012b). Leading edge vortex in a slow-flying passerine. *Biol. Lett.* **8**, 554-557. doi:10.1098/rsbl.2012.0130

Noca, F. (1997). On the evaluation of time-dependent fluid-dynamics forces on bluff bodies. PhD thesis, California Institute of Technology, Pasadena, CA.

Norberg, R. Å. (1975). Hovering flight of the dragonfly *Aeschna juncea* L., kinematics and aerodynamics. In *Swimming and Flying in Nature* (ed. T. Y. T. Wu, C. J. Brokaw and C. Brennen), pp. 763-781. Boston, MA: Springer.

Norberg, U. M. (1975). Hovering flight in the pied flycatcher (*Ficedula hypoleuca*). In *Swimming and Flying in Nature* (ed. T. Y. T. Wu, C. J. Brokaw and C. Brennen), pp. 869-881. Boston, MA: Springer.

Pennycuick, C. J. (1968). Power requirements for horizontal flight in the pigeon *Columba livia*. *J. Exp. Biol.* **49**, 527-555. doi:10.1242/jeb.49.3.527

Pennycuick, C. J., Alerstam, T. and Hedenström, A. H. (1997). A new low-turbulence wind tunnel for bird flight experiments at Lund University, Sweden. *J. Exp. Biol.* **200**, 1441-1449. doi:10.1242/jeb.200.10.1441

Pournazeri, S., Segre, P. S., Princevac, M. and Altshuler, D. L. (2013). Hummingbirds generate bilateral vortex loops during hovering: evidence from flow visualization. *Exp. Fluids* **54**, 1439. doi:10.1007/s00348-012-1439-5

Sane, S. P. and Dickinson, M. H. (2001). The control of flight force by a flapping wing: Lift and drag production. *J. Exp. Biol.* **204**, 2607-2626. doi:10.1242/jeb.204.15.2607

Scarano, F. (2013). Tomographic PIV: Principles and practice. *Meas. Sci. Technol.* **24**, 012001. doi:10.1088/0957-0233/24/1/012001

Shinde, S. Y. and Arakeri, J. H. (2018). Physics of unsteady thrust and flow generation by a flexible surface flapping in the absence of a free stream. *Proc. R. Soc. A Math. Phys. Eng. Sci.* **474**, 20180519. doi:10.1098/rspa.2018.0519

Spedding, G. R. and McArthur, J. (2010). Span efficiencies of wings at low Reynolds numbers. *J. Aircr.* **47**, 120-128. doi:10.2514/1.44247

van den Berg, C. and Ellington, C. P. (1997). The vortex wake of a 'hovering' model hawkmoth. *Philos. Trans. R. Soc. B Biol. Sci.* **352**, 317-328. doi:10.1098/rstb.1997.0023

Vejdani, H. R., Boerma, D. B., Swartz, S. M. and Breuer, K. S. (2018). The dynamics of hovering flight in hummingbirds, insects and bats with implications for aerial robotics. *Bioinspir. Biomim.* **14**, 016003. doi:10.1088/1748-3190/aaea56

Wakeling, J. M. and Ellington, C. P. (1997). Dragonfly flight. III. Lift and power requirements. *J. Exp. Biol.* **200**, 583-600. doi:10.1242/jeb.200.3.583

Warfvinge, K. (2019). Power and wake dynamics of hawkmoth flight. *PhD thesis*, Lund University. ISBN 978-91-7895-142-0.

Warfvinge, K., KleinHeerenbrink, M. and Hedenström, A. (2017). The power–speed relationship is U-shaped in two free-flying hawkmoths (*Manduca sexta*). *J. R. Soc. Interface* **14**, 20170372. doi:10.1098/rsif.2017.0372

Warfvinge, K., Johansson, C. and Hedenström, A. (2021). Hovering flight in hummingbird hawkmoths: kinematics, wake dynamics and aerodynamic power. *Dryad, Dataset*, doi:10.5061/dryad.fqz612jpx

Warrick, D. R., Tobalske, B. W. and Powers, D. R. (2005). Aerodynamics of the hovering hummingbird. *Nature* **435**, 1094-1097. doi:10.1038/nature03647

Weis-Fogh, T. (1973). Quick estimates of flight fitness in hovering animals, including novel mechanisms for lift production. *J. Exp. Biol.* **59**, 169-230. doi:10.1242/jeb.59.1.169

Willmott, A. P. and Ellington, C. P. (1997). The mechanics of flight in the hawkmoth *Manduca sexta*. I. Kinematics of hovering and forward flight. *J. Exp. Biol.* **200**, 2705-2722. doi:10.1242/jeb.200.21.2705

Wolf, M., Ortega-Jimenez, V. M. and Dudley, R. (2013). Structure of the vortex wake in hovering Anna's hummingbirds (*Calypte anna*). *Proc. R. Soc. B: Biol. Sci.* **280**, 20132391. doi:10.1098/rspb.2013.2391
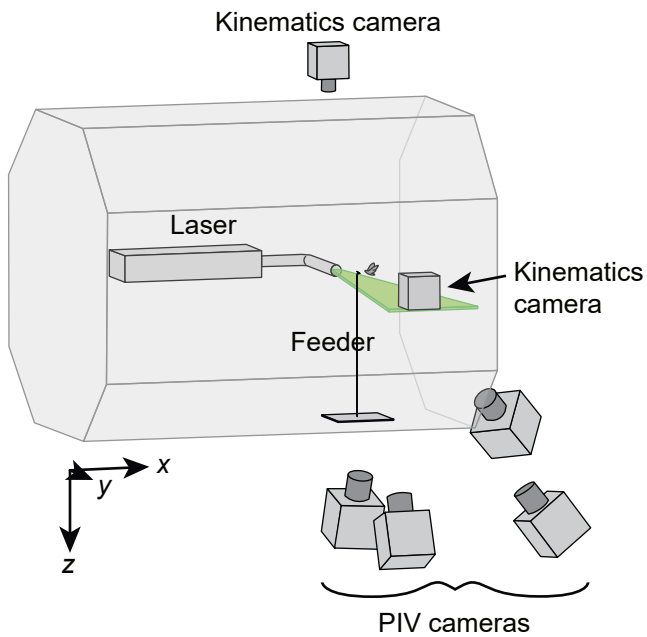
Figure S1. Experimental setup. A *M. stellatarum* is hovering in front of a feeder in the 1.2 m wide test section of the Lund University wind tunnel while two kinematics cameras are recording its flight. Simultaneously a PIV system, consisting of a laser, an aerosol generator (not in view) and four cameras, records the air flow below the moth. The figure is not to scale.
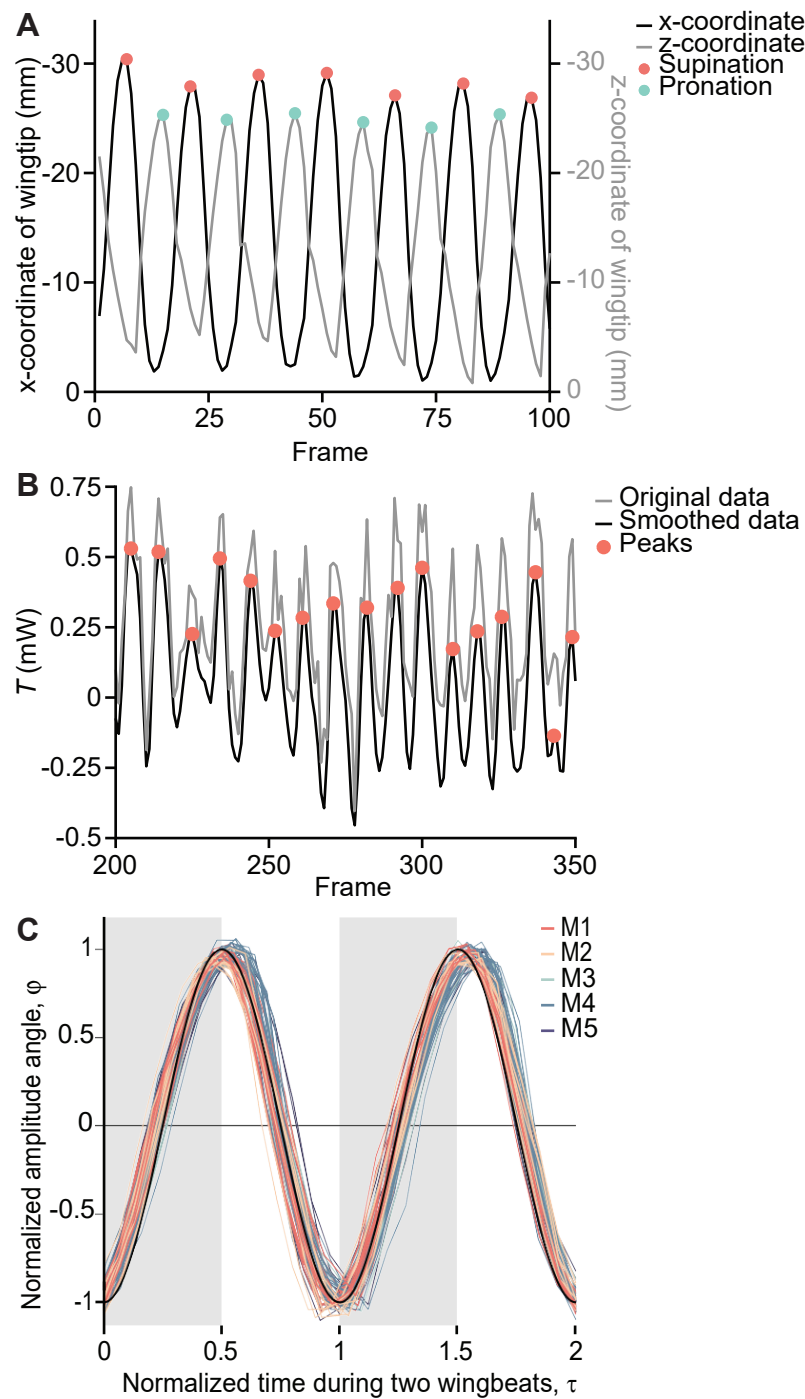
Figure S2. (A) Signals used to determine start of downstroke and upstroke. Start of the down-stroke was defined as the minimum z-coordinate, which was the highest point of the wingbeat. Start of the upstroke was defined as the minimum x -value, which represented the forward- most point of the wing tip during a wingbeat. This sequence is based on one flight of individual M1. **(B)** The signal used for detecting wingbeats (grey line, Eq. 20) along with its smoothed version (black line). The peaks in the smoothed signal, here highlighted by red dots, were interpreted as start and stop of the wingbeats. The moth (individual M1) is here flying at 0.3 ms^{-1}, and conse-quently we do not expect this component of thrust to average to zero. **(C)** Normalized stroke angle (φ) over normalized time (τ) of two wingbeats. Included are all wingbeats in the dataset, recorded with the feeder at the default, low position. Black line is a sine wave ($\varphi = \sin(2\pi\tau - \pi/2)$). Grey area is down-stroke, and white area upstroke.
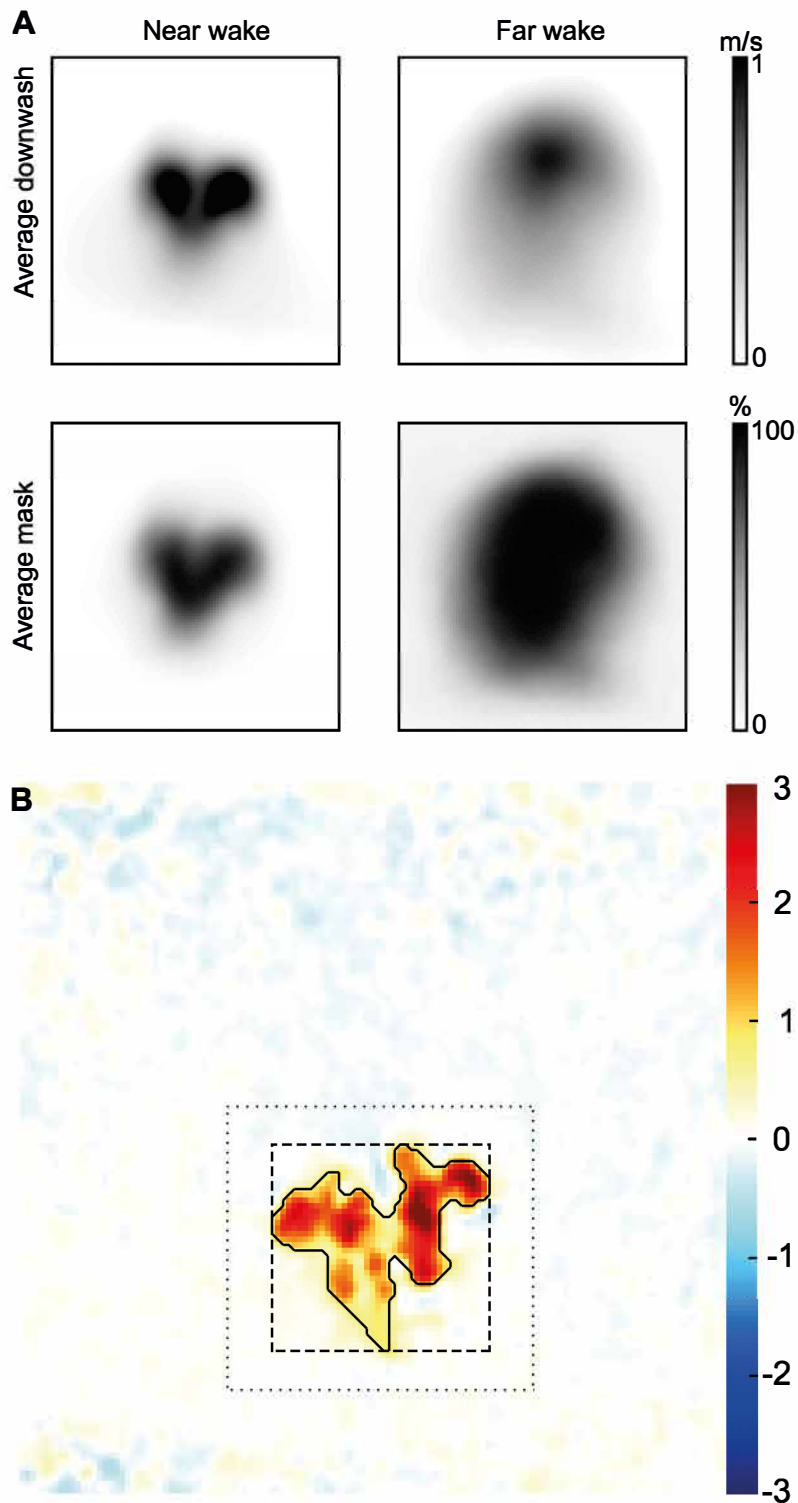
Figure S3. (A) The top row depicts average downwash of all flight sequences in the near and far wake experiments. The images are seen from above, with the moth directed towards the top of the image. The average masks created from the downwash are shown in the second row. The colour represents the percentage of all frames that include a certain pixel in the mask, so that a black pixel is present in 100% of all masks. Before averaging, all wakes were centered. **(B)** One frame of the w velocity field along with the three versions of wake masking: Black line is the mask used for all calculations, dashed line the tightly fitted rectangle and dotted line a rectangle 40% larger in both directions. Colour bar is in ms^{-1}.
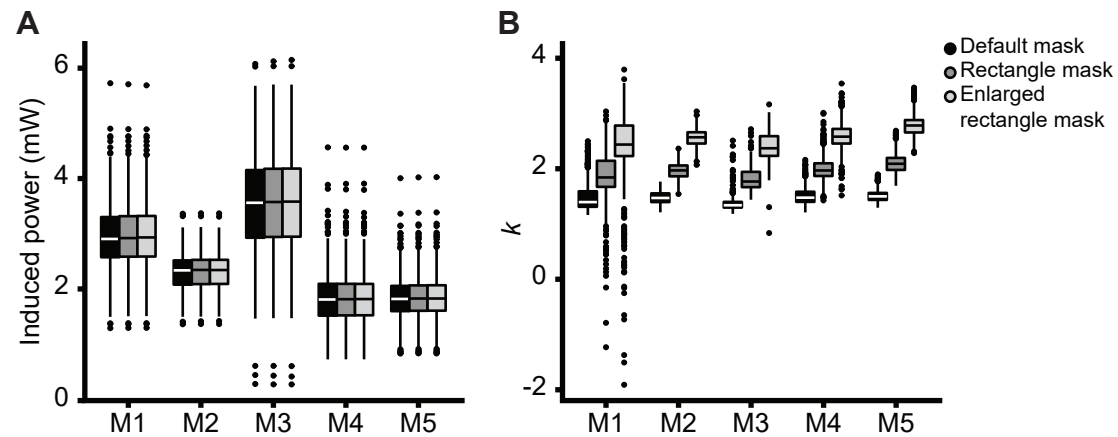
Figure S4. Induced power (A) and k (B) estimated from the PIV data, using three different mask sizes (see Fig. S5). Each wingbeat represents one data point.

Table S1. Morphological characteristics of the individuals used: weight (W) estimated from average lift with standard deviation (s.d.) of measurements, wing area (S), wing span (b), mean wing chord (c), aspect ratio (AR) estimated sensu Pennycuick 1968 and number of sequences (# seq) used in the analyses for each of the moths at the different feeder locations.

Individual	W (mN) avg.	s.d.	S (mm²)	b (mm)	c (mm)	AR	# seq Low feeder Kin	# seq Low feeder PIV	# seq High feeder
M1	3.1	0.64	411	49.2	8.4	5.9	5	6	
M2	3.0	0.38	356	43.4	8.2	5.3	3	2	
M3	3.7	0.67	339	46.2	7.3	6.3	4	4	
M4	2.5	0.58	291	43.6	6.8	6.2	6	4	3
M5	2.4	0.45	327	45.5	7.3	6.1	5	4	3

Table S2. Average and standard deviation of kinematic parameters measured in sequences with the standard feeder placement (40 mm above laser sheet): wingbeat frequency (*f*), wingbeat amplitude (*Φ*), stroke plane angle *θ* and body angle *β*. Lower part of the table shows average of kinematic parameters measured in sequences with the standard feeder placement ("low") as well as with the feeder placed 140 mm above the sheet ("high")

Individual	*f* (Hz)		*Φ* (°)		*θ* (°)		*β* (°)	
	avg.	s.d.	avg.	s.d.	avg.	s.d.	avg.	s.d.
M1	68.9	5.3	96.4	8.0	33.4	6.8	34.8	8.5
M2	69.2	4.3	96.3	5.2	32.4	3.2	28.7	3.7
M3	83.3	3.6	82.2	3.8	30.8	2.2	36.4	2.7
M4	75.4	4.5	91.7	6.8	34.5	4.6	39.1	4.7
M5	74.9	3.8	89.5	6.3	33.2	4.9	39.4	4.7
	Low	High	Low	High	Low	High	Low	High
M4	75.4	80.2	91.7	97.8	34.5	19.6	39.1	52.3
M5	75.0	75.0	92.1	92.1	31.7	31.7	37.9	37.9